Journal of Alloys and Compounds 1037 (2025) 182406

Contents lists available at ScienceDirect

Journal of Alloys and Compounds

journal homepage: www.elsevier.com/locate/jalcom

Polydopamine-derived carbon-coated reduced graphene oxide microspheres comprising layered double hydroxide-derived binary metal selenide nanocrystals as high-performance anodes for sodium-ion batteries

Jae Seob Lee [a,b,1], Dong Guk Ryu [a,1], Rakesh Saroha [a,c], Sung Woo Cho [a], Gi Dae Park [d,*], Chungyeon Cho [e,*], Jung Sang Cho [a,f,g,**]

[a] Department of Engineering Chemistry, Chungbuk National University, Chungbuk 28644, Republic of Korea
[b] Department of Materials Science and Engineering, Korea University, Anam-Dong, Seongbuk-Gu, Seoul 02841, Republic of Korea
[c] Department of Materials Science and Engineering, Ajou University, Suwon 16499, Republic of Korea
[d] Department of Advanced Materials Engineering, Chungbuk National University, Chungbuk 28644, Republic of Korea
[e] Department of Biomedical Materials Science, Jeonbuk Advanced Bio-convergence Academy, Wonkwang University, Iksan, Jeonbuk 54538, Republic of Korea
[f] Biomedical Research Institute, Chungbuk National University Hospital, Chungbuk 28644, Republic of Korea
[g] Advanced Energy Research Institute, Chungbuk National University, Cheongju, Chungbuk 28644, Republic of Korea

ARTICLE INFO

Keywords:
Sodium-ion batteries
Anodes
Spray drying process
Reduced graphene oxide
Layered double hydroxide
Polydopamine coating

ABSTRACT

The designing strategy of structurally robust and highly conductive nanostructures is crucial for advanced energy storage materials. Herein, a novel and systematic structure design strategy is introduced to fabricate the three-dimensional composite microspheres as anodes for high-performance sodium-ion batteries *via* a facile spray-drying process, followed by a controlled selenization step and surface coating process. The hierarchical structure comprises a reduced graphene oxide (rGO) framework integrated with uniformly dispersed bimetallic selenide ($Co_{0.85}Se/MoSe_2$) nanocrystals, encapsulated by N-doped graphitic carbon (NGC) derived from a metal-organic framework serving as a self-sacrificing template, and an additional N-doped carbon layer from polydopamine (PDA-NC). To ensure homogeneous Co–Mo hybridization, CoMo-layered double hydroxide is prepared using a precursor solution containing ZIF-67 and Mo-salts. Subsequent selenization process induces the formation of uniformly dispersed bimetallic selenide nanocrystals, with Co-species facilitating *in-situ* graphitization of N-rich organic ligands to form NGC. The rGO framework within the nanostructure serves as a primary electron transport network, while NGC provides a secondary electron transport pathway between the active nanocrystals and rGO matrix, significantly improving charge carrier mobility. The incorporation of bimetallic selenides offers superior electrochemical properties compared to their monometallic counterparts due to enhanced redox kinetics and synergistic effects between $Co_{0.85}Se$ and $MoSe_2$. The final PDA-NC layer further enhances the structural integrity of the overall structure and electrical contact between the nanostructures at the electrode level. Benefiting from this precisely engineered structure, the optimized anode exhibits exceptional electrochemical performance, demonstrating a high-rate capability up to 7.0 A g^{-1}, extended cycling stability over 300 cycles at 1.0 A g^{-1}, and an improved Na-ion diffusion coefficient of approximately 10^{-13} cm^2 s^{-1}.

1. Introduction

Rechargeable lithium-ion batteries (LIBs) have demonstrated immense potential for portable electronic devices and are increasingly being adopted for large-scale applications, such as electric and hybrid electric vehicles [1,2]. However, critical challenges, including the scarcity and uneven distribution of lithium resources, limited energy density, and high production costs, have driven global research efforts toward alternative electrochemical energy storage systems [3,4]. Among monovalent ion-based redox systems, sodium-ion batteries

---

[*] Corresponding authors.
[**] Corresponding author at: Department of Engineering Chemistry, Chungbuk National University, Chungbuk 28644, Republic of Korea.
E-mail addresses: gdpark@chungbuk.ac.kr (G.D. Park), cncho37@wku.ac.kr (C. Cho), jscho@cbnu.ac.kr (J.S. Cho).
[1] These authors contributed equally to this work.

https://doi.org/10.1016/j.jallcom.2025.182406
Received 30 April 2025; Received in revised form 11 July 2025; Accepted 20 July 2025

(SIBs) have emerged as a promising alternative to LIBs, primarily due to the abundance and cost-effectiveness of sodium resources [5,6]. However, the larger ionic radius of sodium (1.02 Å) compared to lithium (0.76 Å) results in sluggish reaction kinetics, leading to poor rate performance and inferior cycling stability [7,8]. Therefore, the development of high-performance anode materials with superior electrical conductivity and structural stability is crucial for enhancing the rate capability and long-term cycling performance for SIBs [9,10].

Layered double hydroxide (LDH) nanostructures have recently garnered significant attention for energy storage applications due to their unique structural characteristics, including high redox activity, low toxicity, and excellent stability [11–13]. These nanostructures are classified as two-dimensional (2D) layered materials, formed by the intercalation of one metal hydroxide layer within another. This distinctive architecture offers several advantages: (1) tunable morphology by varying the metal cations and anions within the layered framework, (2) high specific capacities due to the layered structure accommodating numerous sodium ions, and (3) efficient charge distribution within hydroxide layers enhancing charge transport [14–16]. Nevertheless, critical challenges such as poor electronic conductivity ($<10^{-3}$ S cm^{-1}) and severe aggregation of hydroxide layers hinder their widespread use as SIB anode materials [17–19].

To address these challenges, the synthesis of LDH derived from metal-organic frameworks (MOFs) has been explored. MOFs typically consist of a central metal-ion coordinated with organic ligands, forming a three-dimensional (3D) framework [20,21]. This unique 3D architecture not only enhances electrochemical performance but also provides structural stability, making MOFs widely applicable in energy storage systems such as SIBs, oxygen evolution reactions, and Li-sulfur batteries [22–24]. Moreover, MOF-derived LDHs can be easily transformed into transition metal chalcogenide phases with various advantages as SIB anode materials. Particularly, transition metal selenides have attracted increasing attention due to their high theoretical capacities, weak metal–selenium bonding facilitating Na-ion insertion/extraction, and superior electronic conductivity compared to sulfides or oxides [25–27]. For instance, Wang et al. synthesized Co-Co LDH-derived $CoSe_2$ nanocrystals embedded within N-doped carbon nanospheres as anode materials for SIBs, reporting an initial discharge capacity of 465.6 mA h g^{-1} at a current density of 0.1 A g^{-1}, along with excellent high-rate performance up to 5.0 A g^{-1} [28]. The high capacity of the Co-Co LDH nanostructure was attributed to its considerable specific surface area and the structural stability provided by the N-doped hollow carbon nanostructure. Among the various transition metal selenide phases, $Co_{0.85}Se$ and $MoSe_2$ have been shown to provide complementary advantages: $Co_{0.85}Se$ offers high electrical conductivity and fast redox kinetics, while $MoSe_2$ contributes large interlayer spacing and rich active sites, favoring Na-ion intercalation and structural buffering [26,27]. Additionally, bimetallic chalcogenide systems have demonstrated pronounced synergistic effects, including enhanced electron and ion transport, suppressed volume expansion, and stable conversion/intercalation reactions during cycling [27]. These synergistic interactions effectively alleviate particle aggregation and mitigate mechanical strain during continuous Na-ion insertion/extraction cycles, leading to improved long-term electrochemical performance. For example, Guan and co-workers synthesized a multicomponent anode material comprising Co/Ni-based LDH nanocubes *via* a hydrothermal technique followed by sulfidation [29]. The as-prepared hollow CoS_2/NiS_2-LDH nanocubes, when used as an SIB anode, delivered an initial discharge capacity of 802 mA h g^{-1} at 0.1 A g^{-1} and demonstrated stable cycling performance even at a high current density of 5.0 A g^{-1}.

Despite these benefits, transition metal selenides (TMSe) still suffer from issues like volume changes and particle pulverization during cycling, leading to capacity fading [30–32]. Among various strategies developed to address these challenges, combining TMSes with conductive carbon frameworks has emerged as particularly effective. Carbon-based materials, including N-doped carbon and graphitic carbon frameworks, significantly enhance electrical conductivity, provide robust structural stability, and establish efficient electron and ion transport pathways within electrodes. For instance, N-doped carbon frameworks derived from MOFs improve electrical conductivity due to N-doping, creating additional active sites and boosting charge carrier density, effectively mitigating the intrinsic conductivity limitations of transition metal selenides [30]. Graphitic carbon frameworks, on the other hand, provide structural support that mitigates mechanical strain induced by volume changes during cycling, significantly improving electrochemical performance and prolonging battery life [32]. Such carbon frameworks synergistically cooperate with the active chalcogenide phases, mitigating mechanical degradation and improving charge transfer efficiency, ultimately enhancing the long-term electrochemical performance of SIBs.

Based on the aforementioned challenges and strategies, a novel and systematic structure design strategy is introduced to fabricate the multicomponent three-dimensional hybrid anode for SIBs *via* a scalable spray drying technique, followed by controlled selenization and carbon coating process. The spray drying approach not only enables uniform microsphere formation with well-dispersed multicomponent precursors, but also offers significant advantages in terms of process scalability, environmental friendliness, and compositional homogeneity compared to conventional liquid-phase methods. Building upon these advantages, a systematic structural design strategy is applied to engineer a hierarchical microspherical architecture, in which polydopamine-derived N-doped carbon (PDA-NC)-coated microspheres incorporate a reduced graphene oxide (rGO) framework embedded with bimetallic $Co_{0.85}Se$/$MoSe_2$ nanocrystals (denoted as (Co,Mo)Se/rGO@PDA-NC microspheres). During the synthesis process, the MOF precursor undergoes a phase transformation into a CoMo-LDH in the presence of Mo-salts, ensuring the homogeneous integration of Co and Mo at the atomic level. This homogeneous Co–Mo hybridization facilitates the uniform formation of $Co_{0.85}Se$/$MoSe_2$ nanocrystals during subsequent selenization, addressing the common issue of phase segregation in multicomponent metal selenides. Additionally, the self-supporting rGO framework provides a robust electron transport network as well as stabilizes the MOF-derived components during subsequent heat treatment and electrochemical cycling. Furthermore, the PDA-NC coating serves as an interconnecting bridge between microspheres, facilitating rapid and continuous charge carrier transport while simultaneously mitigating structural collapse induced by volume fluctuations. Consequently, the (Co,Mo)Se/rGO@PDA-NC microspheres exhibit superior electrochemical performance, including high rate capability, extended cycling stability, and enhanced Na-ion diffusion kinetics, demonstrating their potential as next-generation SIB anodes.

2. Experimental

2.1. Chemicals

All the chemicals used for synthesizing the (Co,Mo)Se/rGO@PDA-NC were of analytical grade: Cobalt nitrate hexahydrate ($Co(NO_3)_2 \cdot 6\,H_2O$, Junsei, 98 %, $M_w = 291.02$), 2-methylimidazole (2-mIM, $C_4H_6N_2$, Acros Organics, 99 %, $M_w = 82.10$), triethylamine (TEA, $C_6H_{15}NO_3$, Alfa Aesar, 99 %, $M_w = 101.19$), ammonium molybdate tetrahydrate ($(NH_4)_6Mo_7O_{24} \cdot 4\,H_2O$, Daejung, 98 %, $M_w = 1235.86$), graphite flakes (Aldrich, <20 μm), selenium powder (SAMCHUN, 99.5 %, $M_w = 78.96$), dopamine hydrochloride (Alfa Aesar, 99 %, $M_w = 189.64$) and tris buffer solution (0.01 M, pH: 8.7). The spray solution was prepared using distilled water as the solvent.

2.2. Synthesis process

2.2.1. Preparation of (Co,Mo)Se/rGO@NGC mmicrosphere

Composite microspheres comprising reduced graphene oxide and bimetallic Co_3Se_4/$MoSe_2$ nanocrystals (labeled as (Co,Mo)Se/

rGO@NGC microspheres) were prepared by a facile spray drying process (Scheme S1) followed by selenization. To prepare the spray solution, zeolitic imidazolate framework-67 (ZIF-67) polyhedra were synthesized *via* a solution-based process, as described in a previously reported study [25,33]. Briefly, 0.716 g of $Co(NO_3)_2 \cdot 6\ H_2O$ was dissolved in 50 mL of distilled water, designated as Solution A. Solution B was prepared by dissolving 1.6 g of 2-mIM and 6 mL of TEA in 50 mL of distilled water. Solution A was then poured into Solution B, and the mixed solution was stirred for 1 h at an ambient atmosphere, followed by ripening for 24 h. The ZIF-67 powders were collected by centrifugation after washing 4 times with distilled water and ethanol, and dried in a vacuum oven fixed at 60 ℃. Moreover, graphene oxide (GO) was prepared using a modified Hummer's method [34]. The spray solution was prepared by dispersing 4.422 g of ZIF-67 polyhedra and 0.4 g of GO nanosheets in 200 mL of distilled water, along with dissolving 3.531 g of $(NH_4)_6Mo_7O_{24} \cdot 4\ H_2O$. The molar ratio of Co- and Mo-species in distilled water was fixed as 1:1. The viscosity of the resulting spray solution was measured to be approximately 24 cP using a viscometer. After vigorous stirring for 12 h, the homogeneous suspension was pumped into the spray dryer using a two-fluid nozzle and then atomized at a pressure of 2.0 bar. The inlet and outlet temperatures of the spray dryer were adjusted to 190 and 100 ℃, respectively. Afterward, grayish powders were obtained at a cyclone-type collector and stabilized in an air oven fixed at 150 ℃ for 3 days. Following this, the as-prepared powders were transferred to a crucible together with a small alumina bottle containing Se powder and selenized for 3 h at 350 ℃ under a reducing atmosphere (Ar/H_2 (vol=95:5 %)) to obtain (Co,Mo)Se/rGO@NGC microspheres. The weight ratio of Se powder and as-prepared powders was maintained at 5:1.

2.2.2. Preparation of (Co,Mo)Se/rGO@PDA-NC microspheres

The yielded (Co,Mo)Se/rGO@NGC microspheres (100 mg) were dispersed in 100 mL of tris buffer solution (0.01 M, pH: 8.7); subsequently, 50 mg of dopamine hydrochloride was added to the above solution and stirred for 12 h under ambient conditions. The PDA-coated (Co,Mo)Se/rGO@NGC microspheres were then washed several times with distilled water, collected by centrifugation, and subsequently dried in an air oven at 100 ℃. Finally, (Co,Mo)Se/rGO@PDA-NC microspheres were obtained by heat treatment for 3 h at 400 ℃ in N_2 atmosphere.

2.2.3. Preparation of CoSe/rGO@PDA-NC and (Co,Mo)Se@PDA-NC microspheres

For comparison, composite microspheres without $MoSe_2$ named as CoSe/rGO@PDA-NC were also prepared through an identical process. Notably, the $(NH_4)_6Mo_7O_{24} \cdot 4\ H_2O$-free spray solution with twice the amount (8.844 g) of ZIF-67 to maintain the concentration of metal-cation and 0.4 g of GO to 200 mL of distilled water was used to synthesize the Mo-salt free as-prepared powders. The subsequent procedure was carried out in the same condition. Another comparison sample without GO named as (Co,Mo)Se@PDA-NC microsphere was prepared under identical conditions. The GO-free spray solution contained 4.422 g of ZIF-67 and 3.531 g of $(NH_4)_6Mo_7O_{24} \cdot 4\ H_2O$ to 200 mL of distilled water, subsequently, the procedure is identical as well.

2.3. Characterization techniques

The morphology of the composite microspheres was explored using field emission scanning electron microscopy (FE-SEM, ULTRA PLUS, ZEISS) and field emission transmission electron microscopy (FE-TEM, JEOL, JEM-2100F) at the Korea basic science institute (KBSI) in Daegu. Scanning transmission electron microscopy (STEM) was further performed using a Cs-corrected transmission electron microscope (JEM-ARM200F, NEOARM, with STEM-Cs) at the Center for Research Facilities (CRIEF), Chungbuk National University, to investigate the elemental distribution within the nanostructure. The X-ray diffraction (XRD) measurements were utilized to confirm the phase and crystal structure of the prepared samples using an Empyrean diffractometer with Cu K_α radiation ($\lambda_{avg} = 1.5425$ Å), operated at 40 kV and 30 mA at KBSI Daegu center. The chemical states and electronic structure of the samples were studied by X-ray photoelectron spectrometer (XPS, K-Alpha, Thermo Fisher Scientific) with microfocus monochromated Al K_α radiation at 12 kV and 20 mA. Raman spectroscopy (Horiba Jobin-Yvon, HR800, LabRam) was utilized to investigate the crystallinity of the carbonaceous material in the prepared samples. The surface area of the samples was measured by the Brunauer–Emmett–Teller (BET) method, where N_2 was used as the adsorbate gas. The thermal characteristics and carbon contents of the prepared samples were assessed using thermogravimetric analysis (TGA, Pyris 1, Perkin Elmer) in the range of 25–750 ℃ under an air atmosphere with a ramping rate of 10 ℃ min^{-1}. Additionally, for the quantitative analysis of carbon and nitrogen elements in the prepared samples, elemental analysis (EA, vario MICRO cube, Elementar) technique based on a high-temperature (1200–1400 ℃) combustion method was used.

2.4. Electrochemical measurements

2032-type coin cells were assembled inside an Ar-filled glove box to investigate the SIB performance of the samples. The working electrodes were prepared with a weight ratio of 7:2:1 for the active material, conductive carbon (Super-P), and sodium carboxymethyl cellulose (CMC) as a binder. The slurry was coated onto a Cu substrate using the doctor blade method and subsequently dried overnight in a hot air oven operated at 60 ℃. Na-metal was used as the reference electrode and counter electrode. The circular electrodes (ϕ=14 mm) with a mass loading of ~1.5 mg cm^{-2} (active material mass = 1.6 mg) were punched and transferred into the glove box. Microporous polypropylene films (Celgard 2400) were utilized as separators. The electrolyte was prepared by dissolving 1.0 M $NaClO_4$ in a mixture of ethylene carbonate and dimethyl carbonate with a volume ratio of 1:1 with 5 wt% fluoroethylene carbonate as an additive. The electrochemical performance was assessed through cyclic voltammetry (CV), discharge/charge test, and electrochemical impedance spectroscopy (EIS) analysis. CV analysis was recorded at a scan rate of 0.01 mV s^{-1}. For cycling stability assessment, the assembled cells underwent tests at different current densities, specifically 0.2 and 1.0 A g^{-1}, using the WBCS3000 (WonATech) cycler. Rate capabilities were tested at different current densities varying from 0.1 to 7.0 A g^{-1}. Throughout all electrochemical tests, the voltage window was maintained within the range of 0.01–3.0 V. EIS measurements were performed in the frequency range of 100 kHz–0.01 Hz using the ZIVE SP1 (WonATech) with a signal amplitude of 10 mV.

3. Results and discussion

3.1. Optimization of nanostructure

The detailed formation mechanism of (Co,Mo)Se/rGO@PDA-NC microspheres is illustrated schematically in Scheme 1. Prior to the preparation of the spray solution, GO nanosheets were prepared *via* the modified Hummer's method, while nano-sized ZIF-67 polyhedra were synthesized using TEA as a deprotonation agent, following a previously reported method [25]. The physical characteristics of these precursors were analyzed, as shown in Fig. S1. The GO nanosheets prepared *via* the modified Hummer's method exhibit a characteristic flake-like morphology, as presented in Fig. S1a. In addition, the FE-SEM image of the synthesized ZIF-67 polyhedra (Fig. S1b) confirms their uniform size and well-defined polyhedral shape, with an average diameter of approximately 70 nm. The relatively small particle size can be attributed to the pH increase induced by TEA, which promotes rapid nucleation and limits further crystal growth [35]. This nanoscale size facilitates effective incorporation of ZIF-67-derived products into the microsphere

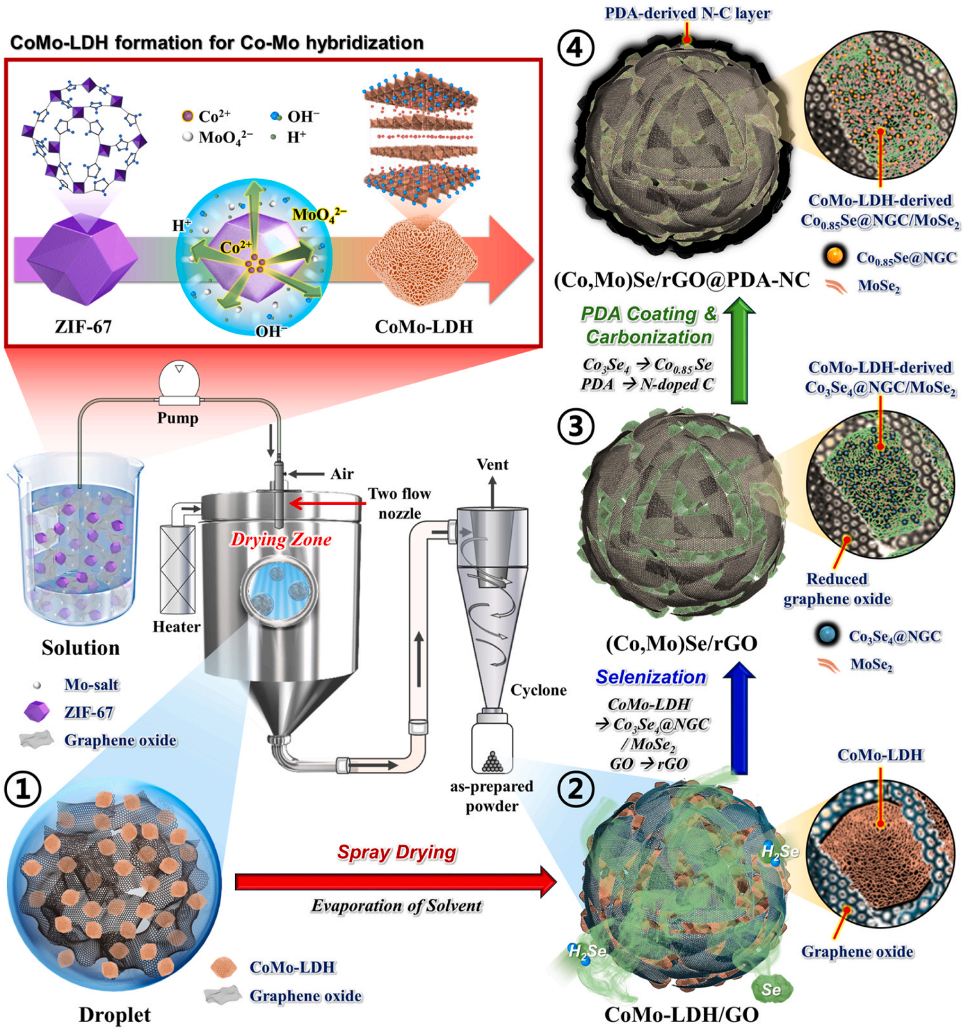

Scheme 1. Schematic representation of the detailed formation mechanism (①–④) of the (Co,Mo)Se/rGO@PDA-NC microspheres.

structure during the spray drying process. Furthermore, the XRD pattern (Fig. S1c) is consistent with previously reported data, indicating the successful formation of ZIF-67 without any detectable impurity phases [36]. To ensure homogeneous Co–Mo hybridization during the preparation of the spray solution, the as-prepared ZIF-67 powders were first dispersed in distilled water to form a purple suspension. Gradual addition and stirring of $(NH_4)_6Mo_7O_{24}$ as a Mo-salt then led to a progressive color change, resulting in a dark blue suspension (Fig. S1d). This color change suggests an ongoing ion-exchange reaction, where the Mo-species from $(NH_4)_6Mo_7O_{24}$ interact with Co-ions in the ZIF-67 structure, initiating its transformation into CoMo-LDH. Specifically, $(NH_4)_6Mo_7O_{24}$ dissociates into NH_4^+, H^+, and MoO_4^{2-} ions in aqueous solution, where MoO_4^{2-} ions gradually disrupt the coordination bonds between Co^{2+} and 2-mIM ligands in ZIF-67, initiating a chemical etching process from the outer surface toward the core [37,38]. This process involves the protonation of 2-mIM ligands, weakening the metal–ligand framework and facilitating the release of Co^{2+} ions into solution [37, 38]. The freed Co^{2+} ions then interact with OH^- and MoO_4^{2-} to form CoMo-LDH nanosheets, which gradually deposit on the surface of the decomposing ZIF-67 polyhedra [37,38]. During this process, a portion of the Co^{2+} ions undergo oxidation to form Co^{3+} ions, as indicated by the dark blue color of the suspension (Fig. S1d). As this reaction progresses, the original ZIF-67 structure undergoes a morphological transformation, with CoMo-LDH progressively replacing the metal-organic framework, leading to the formation of crumpled, sheet-like LDH structures. The resulting suspension was subsequently collected by centrifugation, yielding CoMo-LDH powder, which was further characterized to confirm its structural evolution. The FE-SEM image of the sedimented powder (Fig. S1e) reveals a crumpled, flake-like morphology, distinctly different from the original ZIF-67 polyhedral structure (Fig. S1b), suggesting the occurrence of an ion-exchange-driven transformation. Moreover, the XRD pattern of the stabilized sediment (Fig. S1f) exhibits diffraction peaks corresponding to the Co_3O_4 phase, alongside the characteristic reflections of CoMo-LDH, confirming the successful conversion of exchanged Co^{2+} and Co^{3+} into the corresponding hydroxide and oxide phases [39]. To further investigate the elemental distribution and hybridization between Co and Mo elements within the formed LDH structure, X-ray photoelectron spectroscopy (XPS) depth profiling and scanning transmission electron microscopy (STEM)-energy-dispersive X-ray spectroscopy (EDS) elemental mapping analysis were conducted (Fig. S2). The XPS depth profiling was performed up to a depth of 80 nm, considering the particle size of CoMo-LDH (Fig. S2a). The analysis monitored the signals of Co 2*p*, Mo 3*d*, C 1 *s*, and O 1 *s*. A relatively high concentration of oxygen was observed within the top ~10 nm due to surface oxidation. Beyond this region, the atomic concentrations of Co and Mo remained consistent regardless of increasing depth, suggesting a uniform elemental distribution along the depth direction. Furthermore, STEM-EDS elemental mapping clearly revealed the homogeneous spatial distribution of Co, Mo, O, C, and N elements in the CoMo-LDH, without any signs of local agglomeration or phase separation (Fig. S2b). These findings strongly support the uniform atomic-level hybridization of Co and Mo within the LDH matrix, confirming that the ion-exchange reaction led to a well-integrated bimetallic layered structure. To incorporate CoMo-LDH into a well-dispersed network, the as-prepared GO nanosheets were dispersed into the dark bluish suspension, forming a stable colloidal spray solution. This solution was then aerosolized using a 2-fluid nozzle to generate fine aqueous droplets (Scheme 1-①). The generated droplets contained homogeneously dispersed CoMo-LDH and GO nanosheets in distilled water, ensuring formation of uniform CoMo-LDH/GO composite microspheres after the spray drying process (Scheme 1-②). Moreover, dissolved Co^{3+} ions promote strong interactions between CoMo-LDH and GO nanosheets, contributing to the densification of the microsphere structure. Subsequently, as-sprayed CoMo-LDH/GO composite underwent a selenization process under the Ar/H_2 (vol=95:5 %) atmosphere with Se powders. During the selenization, CoMo-LDH acted as a source for metallic-Co and Mo-species nuclei, which reacted with the H_2Se gas formed due to the combination of H_2 with Se to produce bimetallic selenide phases, specifically Co_3Se_4 and $MoSe_2$ nanocrystals. Simultaneously, the N-rich organic ligands within the LDH matrix facilitated *in-situ* N-doping of the carbonaceous species present in the precursors. The Co-species, reduced to metallic nanoparticles under the selenization conditions, catalyzed the transformation of disordered carbon into graphitic structures through a dissolution–precipitation mechanism [40,41]. In this process, thermally decomposed carbon atoms were adsorbed onto the Co surface, diffused, and subsequently precipitated as ordered graphitic layers. This also enabled the incorporation of nitrogen into the carbon lattice, leading to the formation of NGC on the surface of Co-species. Meanwhile, the GO nanosheets were thermally reduced to rGO. This structural evolution resulted in a robust rGO-based composite framework, in which the well-embedded Co_3Se_4@NGC and $MoSe_2$ nanocrystals were uniformly distributed (Scheme 1-③). In the final step, a conformal PDA-NC layer was uniformly coated onto the (Co,Mo)Se/rGO microspheres *via* a facile solution-based polymerization process. The coated microspheres were subsequently carbonized at 400 ℃ for 3 h under an inert N_2 atmosphere. This post-treatment led to the further reduction of Co_3Se_4@NGC into $Co_{0.85}Se$@NGC nanocrystals while simultaneously forming a uniform PDA-NC shell around the microspheres, leading to the formation of (Co,Mo)Se/rGO@PDA-NC microspheres (Scheme 1-④). This phase transformation from Co_3Se_4 to $Co_{0.85}Se$ is mainly driven by the interaction between oxygen-containing functional groups (e.g., phenolic or quinonoid groups) in the PDA coating and selenium atoms in the Co_3Se_4 lattice. Upon annealing, these oxygen moieties react with selenium to form volatile SeO_2, which readily evaporates at ∼315 ℃ [42]. The resulting

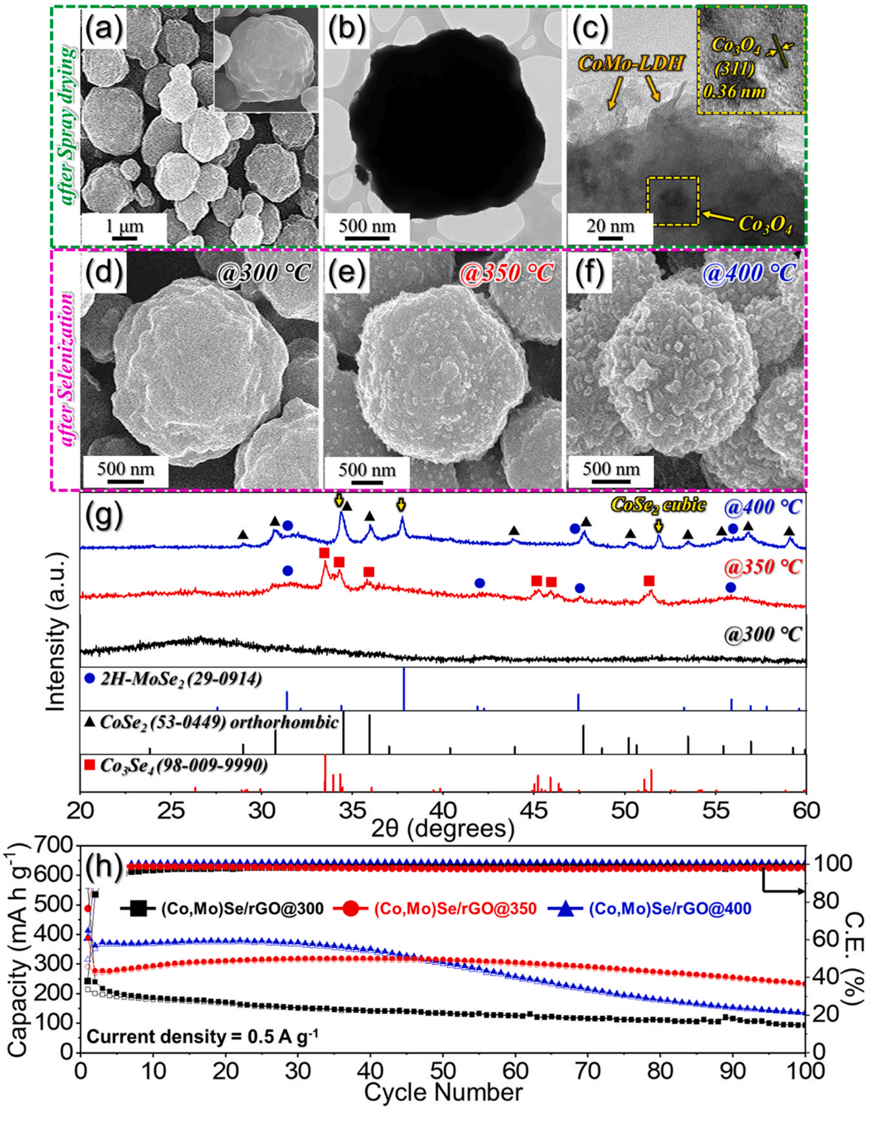

Fig. 1. Morphological, crystal structure, and electrochemical characterizations of (a–c) as-sprayed composite microspheres and (d–h) after selenization at various temperatures under H_2/Ar atmosphere: (a) FE-SEM micrograph, (b) TEM image, and (c) HR-TEM image, (d–f) FE-SEM micrographs, (g) XRD patterns obtained at various selenization temperature, and (h) cycling performance at a current density of 0.5 A g^{-1}.

selenium loss induces a phase shift to the Se-deficient $Co_{0.85}Se$. Therefore, the overall synthesis process generated robust 3D microspheres with improved structural integrity and interconnected conductive networks to ensure long-term electrochemical stability and support fast charge transport kinetics.

To investigate the morphological and structural variations during synthesis, a detailed analysis was conducted at each stage. The as-sprayed CoMo-LDH/GO composite microspheres were characterized in terms of their morphology, crystal structure, and bonding characteristics (Fig. 1a–c and Fig. S3). The FE-SEM micrograph (Fig. 1a) shows that the microspheres exhibit a uniform spherical morphology with an average diameter of approximately 2.5 μm, confirming their structural uniformity. They are well-dispersed without significant aggregation, indicating the effectiveness of the spray drying process in forming discrete particles. The inset of Fig. 1a provides a high-magnification view of a single microsphere, revealing a distinct wrinkled texture on its surface, with no visible deposits, suggesting that the precursor components are well-confined within the microsphere architecture. TEM analysis further supports these observations. The TEM image (Fig. 1b) verifies spherical morphology with a dense structure, indicative of tightly integrated components. The magnified TEM image (Fig. 1c) reveals the presence of sheet-like nanocrystals, corresponding to the CoMo-LDH phase. Additionally, the inset of Fig. 1c displays distinct lattice fringes with a spacing of 0.36 nm, assigned to the (311) atomic plane of Co_3O_4. This oxide phase formation is attributed to the partial oxidation of CoMo-LDH and Co^{3+} ions induced by prolonged stabilization following spray drying. To further investigate the crystalline properties, XRD analysis was conducted (Fig. S3a). The diffraction peaks at approximately $2\theta = 8.7^\circ$ and 33.7° confirm the presence of the CoMo-LDH phase, while a broad hump at $2\theta = 25.4^\circ$ corresponds to the carbonaceous framework formed by GO. Additionally, low-intensity peaks assigned to Co_3O_4 further support the partial oxidation of CoMo-LDH and Co^{3+} ions, aligning with TEM observations. Raman spectroscopy (Fig. S3b) was employed to elucidate the bonding environment. Peaks at 359.9 and 591.4 cm^{-1} correspond to Co–O–Mo vibrations and CoOOH, respectively, confirming the presence of CoMo-LDH [43]. Peaks at 809.4 and 925.7 cm^{-1} indicate the presence of O–Mo–O and Mo═O bonds, associated with molybdenum oxide species [43]. Notably, a peak at 683.8 cm^{-1} suggests Mo–C bonding, indicative of interactions between molybdenum species and organic ligands. Additionally, D-band (1326.4 cm^{-1}) and G-band (1575.3 cm^{-1}) peaks are observed, with the G-band confirming GO incorporation [44]. Elemental mapping analysis (Fig. S3c) further verifies the uniform distribution of Co, Mo, C, N, and O elements within the microsphere, confirming the homogeneous integration of CoMo-LDH and GO. These structural insights collectively demonstrate the successful formation of CoMo-LDH/GO composite microspheres with a well-integrated architecture and uniform composition.

The as-sprayed CoMo-LDH/GO powders underwent a selenization process at varying temperatures to investigate the influence of thermal treatment on the morphological, structural, and electrochemical evolution of the composite. The resulting samples were systematically analyzed using FE-SEM, XRD, and electrochemical measurements to determine the optimal nanostructure (Fig. 1d–h). The FE-SEM micrographs in Fig. 1d–f reveal significant morphological transformations as the selenization temperature increases. At 300 ℃ (Fig. 1d), the sample closely resembles the as-sprayed powders (inset of Fig. 1a), maintaining its spherical morphology with no apparent crystalline structures on the surface, suggesting an insufficient degree of phase conversion. However, at 350 ℃ (Fig. 1e), noticeable crystal growth is observed on the microsphere surface, indicating the onset of selenization and the formation of distinct nanocrystalline domains. With further temperature elevation to 400 ℃ (Fig. 1f), the surface crystals become more pronounced, exhibiting larger grain sizes and slight agglomeration, suggesting enhanced crystallization and particle coarsening due to prolonged thermal energy exposure. These morphological changes align with the XRD analysis (Fig. 1g). The XRD pattern of the sample selenized at 300 ℃ exhibits a broad diffraction peak around $2\theta = 26.6^\circ$, corresponding to the carbonaceous framework, while no well-defined peaks associated with metal selenide phases are detected, indicating low crystallinity. In contrast, the sample selenized at 350 ℃ shows distinct diffraction peaks corresponding to the Co_3Se_4 phase, along with broad and low-intensity peaks attributed to the layered 2H-$MoSe_2$ phase. At 400 ℃, a phase transformation occurs, as evidenced by high-intensity diffraction peaks associated with orthorhombic $CoSe_2$, along with additional peaks attributed to cubic $CoSe_2$. The increased intensity and sharpening of these peaks indicate enhanced crystallinity and grain growth, confirming that higher temperatures facilitate phase formation and structural ordering. The electrochemical performance results (Fig. 1h) further corroborate the structural findings. The sample selenized at 350 ℃ demonstrates superior capacity retention of 84 %, significantly higher than those prepared at 300 ℃ (39 %) and 400 ℃ (37 %). Additionally, it exhibits the highest initial Coulombic efficiency of 77 %, indicating improved redox activity and enhanced reversibility. These results suggest that the optimized balance between crystallinity and morphology at 350 ℃ leads to superior electrochemical performance. However, to further enhance electrochemical stability, a carbon coating approach using PDA-NC was applied to the (Co,Mo)Se/rGO composite, as discussed in the following section.

The selenized (Co,Mo)Se/rGO microspheres were further optimized through a PDA-NC coating to enhance structural stability and electrochemical performance. The PDA layer was applied via a solution-based method and carbonized at 400 ℃ under a N_2 atmosphere, forming a conductive N-doped carbon shell. To investigate the effect of PDA content, different amounts of dopamine hydrochloride (20 mg, 50 mg, and 100 mg) were used to coat 100 mg of (Co,Mo)Se/rGO composite microspheres, yielding three PDA-NC-coated samples (PDA 20 mg, PDA 50 mg, and PDA 100 mg). A control sample without PDA-NC (Devoid of PDA) was also analyzed. The physical characterization of the PDA-NC-coated microspheres is shown in Fig. S4. TEM images (Fig. S4a–c) reveal a gradual increase in coating thickness from 14 nm (PDA 20 mg) to 45 nm (PDA 100 mg). EA (Table S1) further supports this trend, showing an increase in carbon content from 11.2 % (uncoated) to 13.0 %, 20.4 %, and 34.3 % for PDA 20 mg, PDA 50 mg, and PDA 100 mg samples, respectively. Similarly, nitrogen content varies from 5.4 % (uncoated) to 4.7 %, 5.8 %, and 7.5 %, with the slight decrease observed in the PDA 20 mg sample attributed to the relative dilution effect caused by increased carbon content. These results confirm the controlled deposition of the N-doped carbon coating, which enhances electrical conductivity and facilitates charge transport by forming a N-doped conductive network. Cycling performance evaluations (Fig. S4d) reveal that the uncoated sample suffered from rapid capacity degradation, while PDA 20 mg improved cycling stability. PDA 50 mg exhibited both higher discharge capacity and superior cycling performance, benefiting from enhanced conductivity and structural reinforcement. At 0.5 A g^{-1}, it retained 89 % of its capacity after 250 cycles, delivering a reversible capacity of 309 mA h g^{-1}, outperforming PDA 20 mg (257 mA h g^{-1}) and PDA 100 mg (233 mA h g^{-1}). Rate capability tests (Fig. S4e) confirm the superior performance of the PDA 50 mg sample across all current densities. The results highlight that optimizing the PDA-NC content is essential to balance structural stability and electrical conductivity. Among the tested samples, PDA 50 mg exhibited the best combination of conductivity, stability, and electrochemical activity, making it the optimal configuration for further analysis. Additionally, to investigate the compatibility of various carbon coating sources with metal selenide-based material systems, traditional pitch coating was also performed on the (Co,Mo)Se/rGO microspheres. Generally, pitch requires a high temperature of over 800 ℃ for transition to carbon, leading to excessive crystal growth and structural collapse of the selenide phase. Therefore, carbonization was performed under a N_2 atmosphere at 400 ℃ to avoid excessive crystal growth of the metal selenide, resulting in incomplete carbonization of pitch (Fig. S5). The pitch-coated sample exhibited a relatively agglomerated morphology by pitch, and the insufficient carbonization led to inferior electrochemical performance compared to the PDA-NC-coated sample. This comparison further confirms the superiority of PDA-NC as a carbon precursor capable of forming uniform carbon coatings, preserving the nanostructure, and enhancing electrochemical activity even at low temperatures.

3.2. Physical characterization of the optimized nanostructure

Based on the above discussion, the (Co,Mo)Se/rGO@PDA-NC microspheres (PDA 50 mg-coated sample) were further analyzed for their detailed morphological, structural, and chemical characteristics. FE-SEM micrographs (Fig. 2a and b) show that the microspheres retain their spherical morphology without noticeable aggregation after PDA-NC coating and carbonization. Compared to the uncoated sample (Fig. 1e), the surface appears smoother and is covered with rounded, soft-looking nanostructures, indicating the successful deposition of the PDA-NC layer. TEM images (Fig. 2c and d) further confirm this, revealing a distinct PDA-NC layer with an average thickness of 17 nm surrounding the microsphere. HR-TEM analysis (Fig. 2e and f) provides insights into the crystalline structure. Lattice fringes with spacings of 0.68 nm and 0.27 nm correspond to the (002) and $(22\bar{2})$ planes of the 2H-$MoSe_2$ and $Co_{0.85}Se$ phases, respectively. Additionally, a 0.34 nm spacing, attributed to the (002) plane of NGC, is visible on the $Co_{0.85}Se$ surface, suggesting well-integrated nanostructures. The uniform Co–Mo hybridization via the CoMo-LDH precursor phase is evident, as the metal selenides are intimately composited within the rGO/NGC matrix. Moreover, the presence of the NGC layer indicates that Co-species act as catalysts during carbonization, promoting the graphitization of organic ligand- and PDA-derived carbon [45]. This process also induces the thermal reduction of Co_3Se_4 to $Co_{0.85}Se$ due to the mild reducing effect of the carbon layer. In addition, the NGC layer ensures the fast transfer of charge carriers during redox reactions, thereby facilitating better electrochemical activity. The crystalline properties of the optimized sample were further analyzed using SAED and XRD. The SAED pattern (Fig. 2g) exhibits characteristic diffraction rings corresponding to NGC/rGO, $Co_{0.85}Se$, and 2H-$MoSe_2$, aligning well with the XRD pattern (Fig. 2h). Raman spectroscopy (Fig. 2i) further confirms the presence of carbonaceous species. Distinct D-band (1358 cm^{-1}), G-band (1568 cm^{-1}), and 2D-band (2805 cm^{-1}) peaks are observed, associated with sp^3-bonded (disordered) carbon, sp^2-bonded (graphitic) carbon,

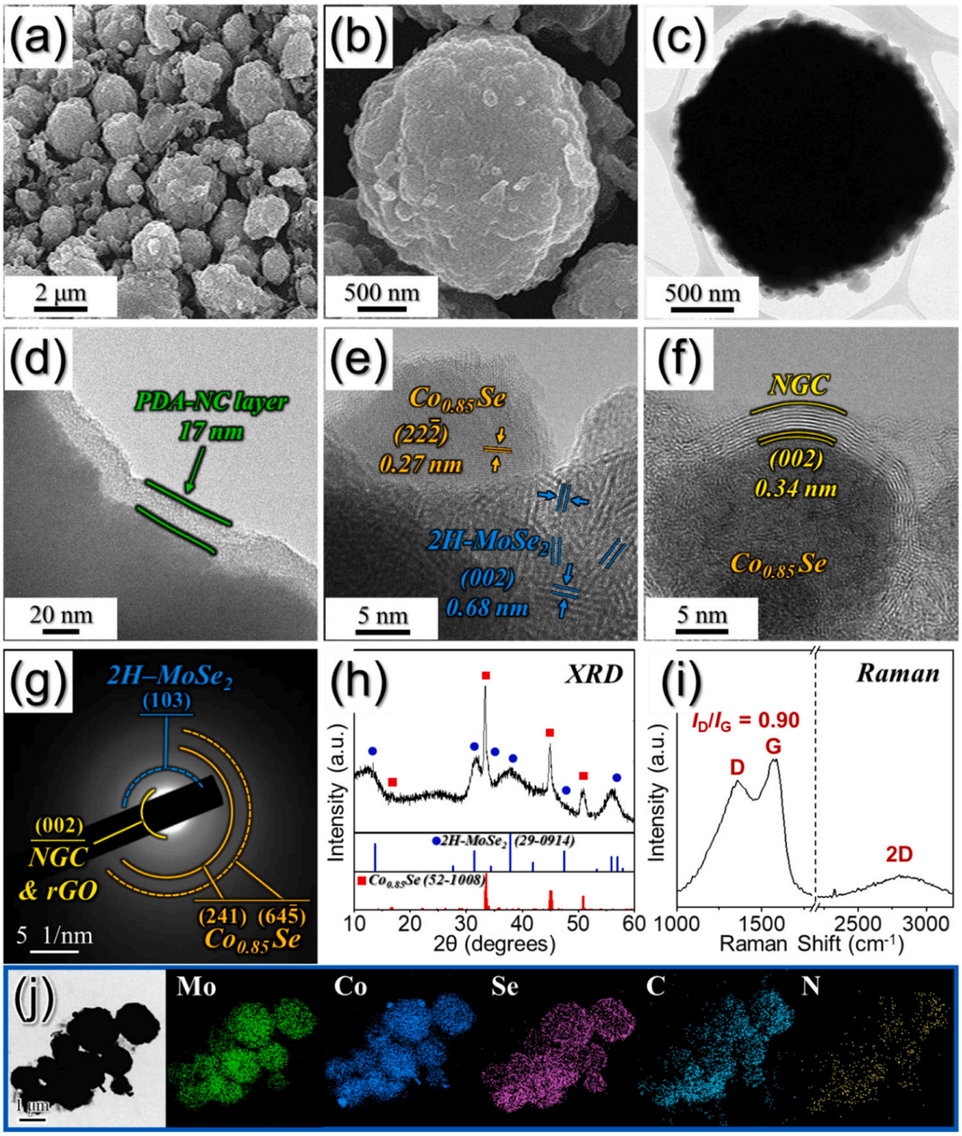

Fig. 2. Physical characterizations of the (Co,Mo)Se/rGO@PDA-NC microspheres: (a, b) FE-SEM micrographs, (c, d) TEM images, (e, f) HR-TEM images, (g) SAED pattern, (h) XRD pattern, (i) Raman spectrum, and (j) elemental dot mapping images.

and the overtone of the D-band, respectively [46]. The I_D/I_G ratio of 0.9 indicates a graphitized nature of the carbonaceous species, attributed to the combined effects of rGO incorporation and Co-catalyzed graphitization of the PDA-derived carbon. The well-defined 2D-band at 2805 cm^{-1} further suggests a degree of long-range ordering, originating from the double resonance effect related to graphitic carbon bonding [47]. Elemental dot mapping (Fig. 2j) confirms the homogeneous distribution of Mo, Co, Se, C, and N, supporting the uniform integration of NGC-coated metal selenide phases. This is further validated by the TEM-EDS spectrum (Fig. S6a), consistently demonstrating the presence of these elements. The elemental composition of the sample was quantitatively assessed using inductively coupled plasma optical emission spectroscopy (ICP-OES) analysis, revealing Co and Mo contents of 43 and 57 mol%, respectively (Fig. S6b). Based on the combined EA (Table S1) and ICP-OES (Fig. S6b) results, the estimated phase proportions of $Co_{0.85}Se$, $MoSe_2$, and rGO/NGC in the composite were calculated to be 23.2, 50.6, and 26.2 wt%, respectively.

The electronic state and bonding environment of the prepared nanostructure were also examined using XPS, and the results are presented in Fig. 3a–f. The XPS survey spectrum (Fig. 3a) shows peaks corresponding to Co 2*p*, O 1 *s*, N 1 *s*, C 1 *s*, Mo 3*d*, and Se 3*d* electronic orbitals. The magnified Co 2*p* spectrum (Fig. 3b) displays distinct peaks attributed to the Co $2p_{3/2}$ and Co $2p_{1/2}$ spin-orbit doublets, accompanied by satellite peaks (marked as '*Sat.*') [48,49]. The deconvoluted Co $2p_{3/2}$ and Co $2p_{1/2}$ spectra reveal photoelectron peaks at 781.0/796.6 and 778.5/793.7 eV, associated with Co^{2+} and Co^{3+} oxidation states, respectively, attributed to the $Co_{0.85}Se$ phase in the nanostructure [50]. Similarly, the Mo 3*d* spectrum (Fig. 3c) shows well-defined peaks at 228.4/231.7 eV and 232.8/235.0 eV, corresponding to Mo–Se and Mo–O species, respectively, with the latter arising from surface oxidation [51]. Additionally, a low-intensity peak at 229.3 eV is attributed to the Se 3 s orbital, confirming the presence of Se-species in the nanostructure [42,52]. The high-resolution Se 3*d* spectrum (Fig. 3d) reveals closely spaced peaks at 53.9 and 54.7 eV, which correspond to the $3d_{3/2}$ and $3d_{5/2}$ spin-orbit doublets of Mo–Se species [53,54]. Additionally, two well-fitted peaks at 59.1 and 60.6 eV are associated with Se–O species, formed due to surface oxidation during measurement [44,54]. Further analysis of the carbon matrix was performed through C 1 *s* and N 1 *s* spectra. The C 1 *s* spectrum (Fig. 3e) reveals fitted peaks at 284.4, 285.2, and 287.8 eV, corresponding to C═C (sp^2 graphitic carbon), C–N/C–C, and O–C═O bonds, respectively [55]. The dominant C═C peak confirms the graphitic nature of the carbon species, while the presence of C–N/C–C bonds suggests N-doping in the carbon matrix, which enhances electronic conductivity of the nanostructure due to the higher electronegativity of nitrogen compared to carbon [56]. The N 1 *s* spectrum (Fig. 3f) further supports the incorporation of N-species, showing peaks at 398.3, 400.1, and 402.5 eV, corresponding to pyridinic-N, pyrrolic-N, and graphitic-N, respectively [57,58]. The high intensity of pyridinic-N suggests improved charge transfer capability and redox kinetics. Additionally, low-intensity peaks at 396.4 and 394.1 eV correspond to Mo–N and Mo 3*p* orbitals, respectively, indicating interactions between $MoSe_2$ and the N-doped carbon species [42]. These observations align well with EA results (Table S1), which indicate an N content of 5.8 wt%. To investigate the thermal characteristics and organic content of the composite, TG analysis was conducted in an air atmosphere (Fig. 3g). The initial weight loss from room temperature to 200 ℃ is attributed to the removal of moisture and crystal water within the nanostructure. A significant weight loss from 200 to 435 ℃ occurs due to the oxidation of $Co_{0.85}Se$ and $MoSe_2$ into $CoSeO_x$ and MoO_x, accompanied by SeO_2 gas release. Further oxidation of Co- and

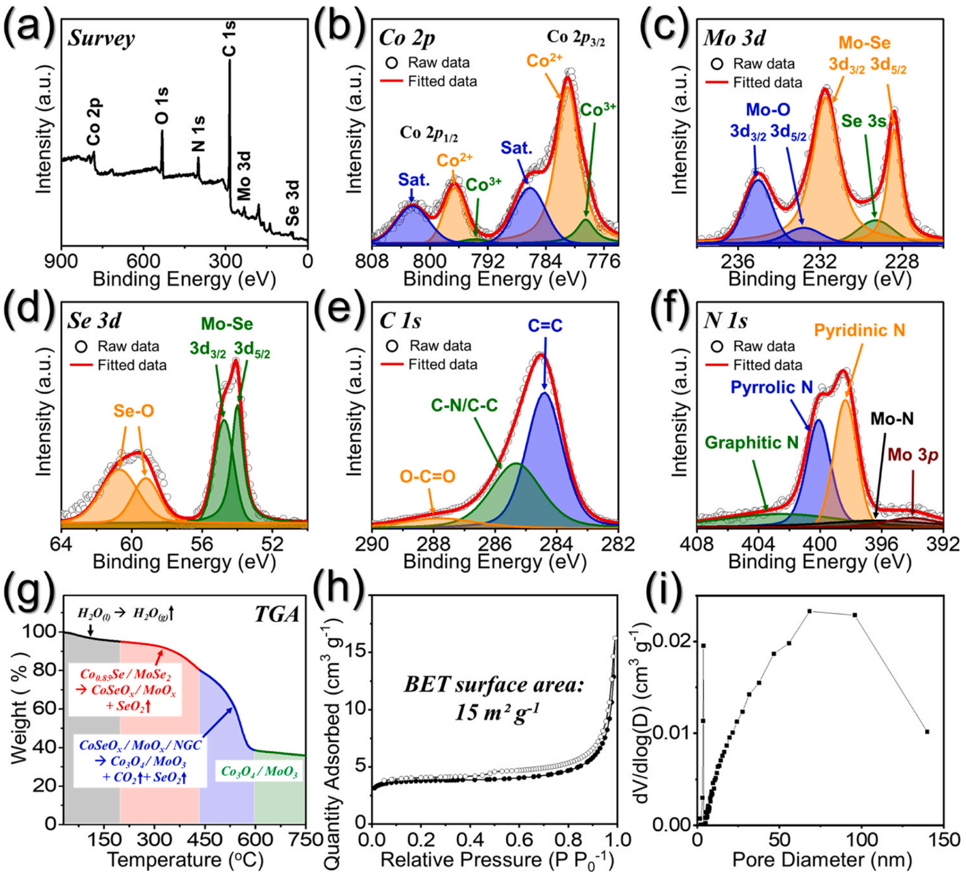

Fig. 3. (a) XPS survey spectrum, (b) Co 2*p*, (c) Mo 3*d*, (d) Se 3*d*, (e) C 1 *s*, (f) N 1 *s* XPS spectra, (g) TG curve, (h) N_2 adsorption–desorption isotherms, and (i) BJH desorption pore size distribution curve of the (Co,Mo)Se/rGO@PDA-NC.

Mo-species continues up to 600 ℃, leading to additional SeO_2 gas release and combustion of carbon species, including rGO and NGC. Beyond 600 ℃, no significant weight loss is observed, indicating the complete conversion of the composite into Co_3O_4 and MoO_3. From the total weight loss, the organic content was estimated to be approximately 27 %, which closely aligns with EA results indicating carbon and nitrogen contents of 20 % and 5.8 %, respectively (Table S1). The porosity characteristics of the (Co,Mo)Se/rGO@PDA-NC microspheres were investigated through N_2 adsorption-desorption isotherms (Fig. 3h). The material exhibited a BET surface area of 15 m^2 g^{-1}, which is relatively low due to the compact structure of the microspheres, as confirmed by TEM analysis. Additionally, the Barrett-Joyner-Halenda (BJH) pore size distribution curve (Fig. 3i) reveals the presence of macropores, although their volume is relatively low. These macropores are primarily attributed to voids between the microspheres. Moreover, a sharp peak near ~4 nm in the BJH pore size distribution curve is observed, which is commonly attributed to the tensile-strength effect [59]. To demonstrate the structural advantages of the (Co,Mo)Se/rGO@PDA-NC microspheres, two control samples were prepared: one without rGO ((Co,Mo) Se/PDA-NC microspheres) and another without the Mo precursor (CoSe/rGO@PDA-NC microspheres). The corresponding physical characterization results, including morphological, structural, and compositional analyses, are presented in Fig. S7 and Fig. S8, along with the relevant discussion.

3.3. Electrochemical performance of the optimized nanostructure

The electrochemical performances of the prepared nanostructures, including CV analysis, charge-discharge voltage profiles, cycling performance, and rate capability tests were evaluated using coin-cell configurations, as shown in Fig. 4a–e. The initial CV profiles, recorded at a scan rate of 0.1 mV s^{-1} within a voltage range of 0.01–3.0 V, are presented in Fig. 4a. During the first cathodic scan, the (Co,Mo)Se/rGO@PDA-NC anode exhibited initial electrochemical activity starting at approximately 1.0 V, corresponding to the Na-ion intercalation into $Co_{0.85}Se$ and $MoSe_2$ phases [26,27,60]. The peak around 0.75 V is attributed to the formation of the solid electrolyte interphase (SEI) layer and the initiation of the conversion reaction of $Na_xCo_{0.85}Se$ into metallic-Co and Na_2Se [26,61,62]. The peaks between 0.5 V and 0.4 V reflect the two-step conversion of Na_xMoSe_2: initially forming intermediate lower selenides (such as $Mo_{15}Se_{19}$) followed by their further conversion into metallic-Mo and additional Na_2Se [27,61,62]. In

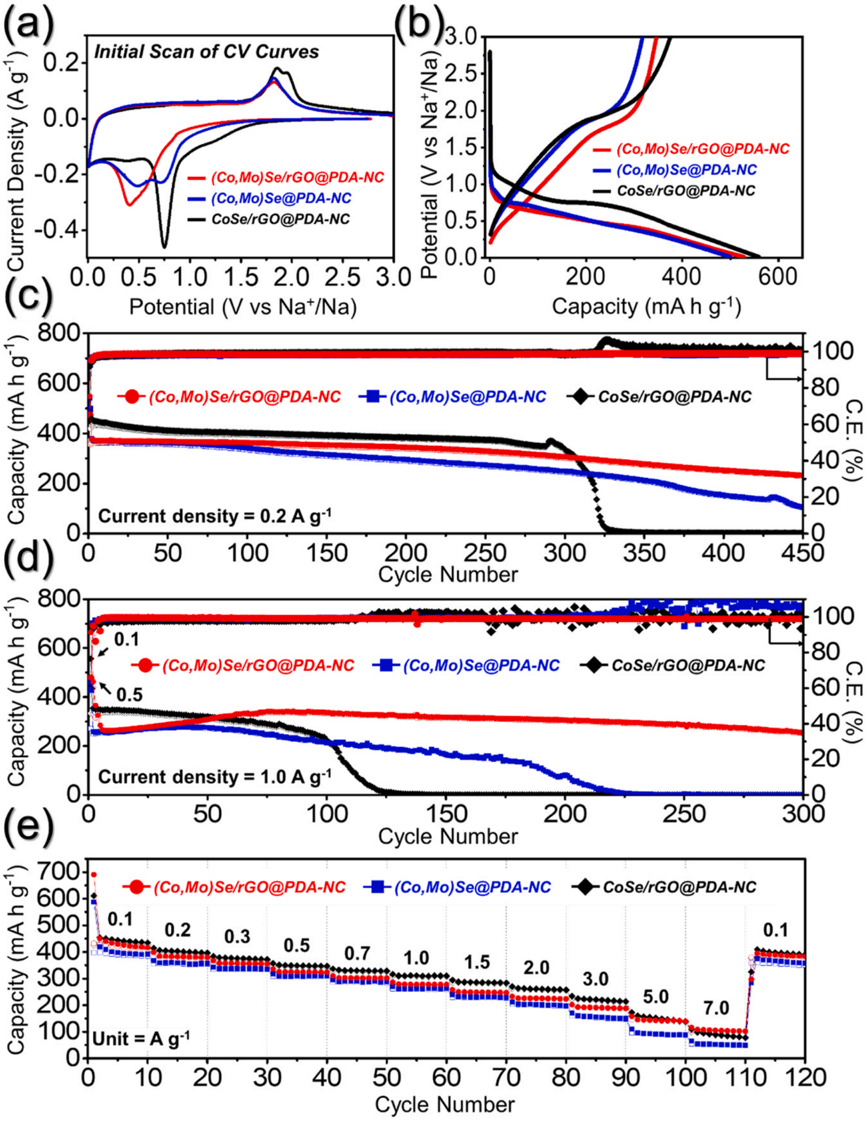

Fig. 4. Electrochemical properties of (Co,Mo)Se/rGO@PDA-NC, (Co,Mo)Se@PDA-NC, CoSe/rGO@PDA-NC anodes for Na-ion storage: (a) initial CV curves at 0.1 mV s^{-1}, (b) initial discharge/charge voltage profiles at current density of 0.1 A g^{-1}, (c) cycling performance at current density of 0.2 A g^{-1}, (d) cycling performance at high current density of 1.0 A g^{-1}, and (e) rate performances.

contrast, the CoSe/rGO@PDA-NC anode, containing Co_3Se_4 and $CoSe_2$ phases, displayed a shoulder peak at 1.2 V, associated with Na-ion intercalation into $CoSe_2$, and a dominant peak at 0.75 V, corresponding to the formation of the SEI layer, Na_2Se, and CoSe from $Na_xCoSe_2/Na_xCo_3Se_4$ [63]. A minor peak at 0.4 V indicates the final conversion of CoSe into Na_2Se and metallic-Co [63]. Meanwhile, the (Co,Mo)Se@PDA-NC anode, comprising Co_3Se_4, $CoSe_2$, and $MoSe_2$ phases, exhibited cathodic peaks at similar voltages but with varying intensities, reflecting the influence of these distinct phases. The presence of $MoSe_2$ in (Co,Mo)Se/rGO@PDA-NC and (Co,Mo)Se@PDA-NC anodes resulted in a peak at 0.5 V, which corresponds to the conversion reaction of $MoSe_2$ [64]. Additionally, the stronger peak intensity at 0.75 V in the (Co,Mo)Se@PDA-NC and CoSe/rGO@PDA-NC anodes compared to (Co,Mo)Se/rGO@PDA-NC anode suggests a higher contribution of Se-rich cobalt selenide phase (Co_3Se_4 and $CoSe_2$), which undergoes a reduction process at this voltage. Furthermore, all samples exhibited an additional peak at 0.03 V, which corresponds to the Na^+ insertion into the carbon matrix, contributing to Na-ion storage within the conductive carbon framework [65,66]. After the first cycle, the initial cathodic peaks disappeared (Fig. S9), indicating that the SEI layer formation primarily occurred during the first cycle. From the second cycle onward, four distinct reduction peaks emerged in all samples. Specifically, the (Co,Mo)Se/rGO@PDA-NC anode exhibited peaks at 1.34, 1.11, 0.72, and 0.03 V, while (Co,Mo)Se@PDA-NC and CoSe/rGO@PDA-NC anodes displayed corresponding peaks at 1.42/1.13/0.72/0.03 V and 1.39/1.10/0.66/0.03 V, respectively. These peaks correspond to distinct electrochemical processes occurring during the reduction cycle. The peak observed at 1.3–1.4 V is associated with Na-ion intercalation and the phase transformation of $Co_{0.85}Se$ and Mo_3Se_4 into their sodiated counterparts, $Na_xCo_{0.85}Se$ and $Na_xMo_3Se_4$, with simultaneous sodiation of metalloid-Se formed during prior cycles [25–27]. As the reaction progresses, the reduction peak at around 1.1 V corresponds to the conversion of $Na_xCo_{0.85}Se$ into metallic-Co and Na_2Se, while the peak at 0.7 V is attributed to the conversion of $Na_xMo_3Se_4$ (*via* $Mo_{15}Se_{19}$ intermediates) into metallic-Mo and Na_2Se [26,27,64]. Finally, a sharp reduction feature at 0.03 V is associated with the Na^+ intercalation into the carbon framework [65]. The anodic scans of all samples (Fig. S9) exhibited similar characteristics, with peaks observed at 0.11/0.11/0.10 V, 0.69/0.40/0.95 V, 1.82/1.82/1.85 V, and 1.90/1.89/1.94 V for (Co,Mo)Se/rGO@PDA-NC, (Co,Mo)Se@PDA-NC, and CoSe/rGO@PDA-NC anodes, respectively. These anodic peaks represent the oxidation processes of metallic-Mo, Co, and deintercalation reactions of Na-ion [64]. The complete reaction mechanism involved during the discharge and charge processes is summarized below.

For the discharge process:

$$Co_{0.85}Se + xNa^+ + xe^- \rightarrow Na_xCo_{0.85}Se \tag{1}$$

$$MoSe_2 + yNa^+ + ye^- \rightarrow Na_yMoSe_2 \tag{2}$$

$$Na_xCo_{0.85}Se + (1-x)Na^+ + (1-x)e^- \rightarrow 0.85Co + Na_2Se \tag{3}$$

$$15Na_yMoSe_2 + zNa^+ + ze^- \rightarrow Mo_{15}Se_{19} + Na_2Se \tag{4}$$

$$Mo_{15}Se_{19} + \omega Na^+ + \omega e^- \rightarrow 15Mo + 19Na_2Se \tag{5}$$

For the charge process:

$$0.85Co + Na_2Se \rightarrow \quad Co_{0.85}Se + 2Na^+ + 2e^- \tag{6}$$

$$15Mo + 19Na_2Se \rightarrow \quad Mo_{15}Se_{19} + 38Na^+ + 38e^- \tag{7}$$

$$Mo_{15}Se_{19} + Na_2Se \rightarrow 5Mo_3Se_4 + 2Na^+ + 2e^- \tag{8}$$

Notably, from the second cycle onward, the CV curves of all samples overlapped significantly, indicating a highly reversible redox process and excellent electrochemical stability. The initial charge-discharge voltage profiles of the prepared anodes at 0.1 A g^{-1} (Fig. 4b) align well with the CV results, confirming the predicted electrochemical reactions. The initial discharge/charge capacities for the (Co,Mo)Se/rGO@PDA-NC, (Co,Mo)Se@PDA-NC, and CoSe/rGO@PDA-NC anodes were 528/345, 499/317, and 559/374 mA h g^{-1}, respectively, with initial Coulombic efficiencies (ICEs) of 65.3 %, 63.5 %, and 66.9 %. Capacity loss in all anodes is primarily due to SEI layer formation and side reactions [67]. Moreover, the voltage polarization from the initial galvanostatic discharge/charge profiles was measured as shown in Fig. S10. The observed polarization values—defined as the voltage difference between charge and discharge plateaus—were 1.34, 1.40, and 1.26 V for the (Co,Mo)Se/rGO@PDA-NC, (Co,Mo)Se@PDA-NC, and CoSe/rGO@PDA-NC anodes, respectively. The lower polarization of the (Co,Mo)Se/rGO@PDA-NC compared to the (Co,Mo)Se@PDA-NC is attributed to the presence of the conductive rGO network, which improves electron transport and reduces internal resistance. Meanwhile, the CoSe/rGO@PDA-NC anode shows the lowest polarization among the three samples, which is consistent with its porous structure and highest specific surface area (Fig. S8e). These features facilitate rapid ion/electrolyte transport and minimize charge-transfer resistance, leading to reduced polarization. Additionally, the higher initial discharge capacity of CoSe/rGO@PDA-NC is attributed to the presence of $CoSe_2$ and Co_3Se_4, which can accommodate more Na-ions compared to the $Co_{0.85}Se$ phase, thereby providing greater sodium storage sites. Additionally, its sparser structure, as shown in Fig. S8c, enhances electrolyte penetration and Na-ion accessibility, further increasing initial capacity. Notably, while the CoSe/rGO@PDA-NC anode exhibits the highest initial discharge/charge capacity, its long-term stability is inferior due to its sparse structure, which may accelerate structural degradation over prolonged cycles, as discussed later. Despite its Se-rich composition ($CoSe_2$ and Co_3Se_4), (Co,Mo)Se@PDA-NC anode shows lower capacity than (Co,Mo)Se/rGO@PDA-NC anode due to the absence of rGO, which otherwise enhances redox reaction kinetics and charge transport efficiency, leading to more effective sodium-ion storage. Moreover, although Co_3Se_4 provides a higher theoretical capacity owing to its higher selenium content, its spinel-like 3D framework with mixed-valence Co centers is structurally rigid and more susceptible to mechanical stress and capacity fading during cycling [68,69]. In contrast, the $Co_{0.85}Se$ phase features a layered structure with superior Na-ion diffusion channels and metallic conductivity, enabling fast, reversible redox reactions and improved cycling stability under practical conditions [26,70,71].

Cycling performance tests were conducted at current densities of 0.2 and 1.0 A g^{-1} to evaluate the structural stability and electrochemical durability of the anodes (Fig. 4c and d). At a current density of 0.2 A g^{-1}, the discharge capacity until 100 cycles follows the order: CoSe/rGO@PDA-NC > (Co,Mo)Se/rGO@PDA-NC > (Co,Mo)Se@PDA-NC, consistent with the higher initial capacity of CoSe/rGO@PDA-NC. However, after 300 cycles, the CoSe/rGO@PDA-NC anode undergoes a sharp capacity drop, leading to complete failure due to structural degradation. In contrast, (Co,Mo)Se/rGO@PDA-NC demonstrates the highest long-term stability, maintaining a discharge capacity of 232 mA h g^{-1} at the 450th cycle, with an average capacity decay rate of 0.08 % per cycle. Meanwhile, the (Co,Mo)Se@PDA-NC anode, despite its Co–Mo hybridization effect from CoMo-LDH precursors, exhibits a gradual decline in reversibility due to the absence of rGO, resulting in a lower 450th cycle capacity of 105 mA h g^{-1} and a higher capacity decay rate of 0.16 % per cycle. The Coulombic efficiency (CE) of (Co,Mo)Se/rGO@PDA-NC (99.0 %) also surpasses that of (Co,Mo)Se@PDA-NC (98.6 %), highlighting the role of rGO in facilitating stable Na-ion insertion/extraction. Similar trends were observed for the three anodes during cycling at a high current density of 1.0 A g^{-1} (Fig. 4d). The (Co,Mo)Se/rGO@PDA-NC anode exhibits an activation period up to 70 cycles due to the dense structure and high current density, leading to a gradual increase in capacity. It retains 255 mA h g^{-1} at the 300th cycle with a high capacity retention of 90 % (corresponding to a low capacity decay rate of 0.003 % per cycle), demonstrating excellent cycling stability. In contrast, the (Co,Mo)Se@PDA-NC anode undergoes activation for 40 cycles but fails after 220 cycles due to progressive capacity fading. The CoSe/rGO@PDA-NC anode, which initially exhibited high capacity due to its sparse structure, fails within just 120 cycles, further emphasizing the importance of structural integrity. To further confirm the role of Co–Mo hybridization in structural stability, Co-species-free MoSe/rGO@PDA-NC microspheres were synthesized following the same procedure without ZIF-67 precursor, and their morphology, crystal phase, and cycling performance were analyzed (Fig. S11). The FE-SEM images revealed that the MoSe/rGO@PDA-NC microspheres were covered with large $MoSe_2$ nanosheets, reflecting pronounced and unrestricted crystal growth during selenization (Fig. S11a). This distinct morphology is attributed to the absence of growth-suppressing factors—the Co-species within CoMo-LDH, ligand-derived NGC, and structural densification induced by Co^{3+} ions. XRD analysis confirmed the formation of the 2H-$MoSe_2$ phase in the MoSe/rGO@PDA-NC (Fig. S11b). Notably, during cycling at 1.0 A g^{-1}, this anode exhibited rapid degradation, with cell failure occurring after 150 cycles, indicating that the absence of Co–Mo hybridization significantly affects cycling stability (Fig. S11c). These results confirm that the superior cycling performance of the (Co,Mo)Se/rGO@PDA-NC anode arises not only from the conductive rGO framework but also from the synergistic interplay between Co- and Mo-species derived from CoMo-LDH, ensuring both high electrical conductivity and structural robustness during long-term operation. To clarify the specific contribution of this bimetallic system, control experiments were conducted using bare $MoSe_2$ and bare $Co_{0.85}Se$, synthesized without rGO or PDA-NC under identical selenization conditions. As shown in Fig. S12a–d, bare $MoSe_2$ exhibited a nanosheet-like morphology and phase-pure 2H-$MoSe_2$, while bare $Co_{0.85}Se$ showed a microspherical morphology with the expected $Co_{0.85}Se$ phase. These single-metal selenides were then electrochemically tested alongside the bimetallic (Co,Mo)Se microspheres (Fig. S7b) at 0.5 A g^{-1} to compare their sodium-storage properties (Fig. S12e). Bare $Co_{0.85}Se$ delivered an initially high capacity (345 mA h g^{-1}) but suffered from rapid fading due to poor structural durability. Conversely, bare $MoSe_2$ showed more stable cycling but lower capacity. In contrast, (Co,Mo)Se microspheres exhibited a balanced profile, with a moderate initial capacity of 280 mA h g^{-1} and superior cycling retention. This behavior highlights the complementary advantages of each component: $Co_{0.85}Se$ contributes high capacity, while $MoSe_2$ provides structural buffering. More importantly, their combination in the form of bimetallic heterostructures enables enhanced redox kinetics and improved ion/electron transport, driven by the formation of interfacial electric fields and abundant lattice mismatches [72–74]. Such heterointerfaces also suppress active material pulverization and promote charge redistribution, further stabilizing the electrode during sodiation/desodiation cycles [72–74]. These findings collectively support that the $Co_{0.85}Se$–$MoSe_2$ synergistic effect significantly contributes to the excellent electrochemical stability and performance of the (Co,Mo)Se/rGO@PDA-NC architecture. Notably, the obtained cycling performance of the (Co,Mo)Se/rGO@PDA-NC anode is comparable to those of previously reported Co- and Mo-based selenide and sulfide anodes for SIBs, as summarized in Table S2.

Rate performance tests were conducted at various current densities ranging from 0.1–7.0 A g^{-1} to assess the power capability of the prepared anodes (Fig. 4e). The (Co,Mo)Se/rGO@PDA-NC and CoSe/rGO@PDA-NC anodes initially exhibited comparable discharge capacities across all current densities. For instance, their capacities at 0.1, 0.2, 0.3, 0.5, 0.7, 1.0, 1.5, 2.0, 3.0, 5.0, and 7.0 A g^{-1} were approximately 417/435, 380/397, 356/372, 324/347, 302/329, 278/311, 248/284, 224/258, 189/214, 139/139, and 102/79 mA h g^{-1}, respectively. However, at high current densities ($\geq$5.0 A g^{-1}), the CoSe/rGO@PDA-NC anode exhibited a significant capacity drop, falling below that of (Co,Mo)Se/rGO@PDA-NC at 7.0 A g^{-1}. This deterioration is attributed to structural instability caused by its sparse morphology, leading to capacity fading under rapid charge/discharge conditions. In contrast, the (Co,Mo)Se@PDA-NC anode, which lacks rGO, demonstrated consistently lower capacities across all current densities, with values of 391, 357, 336, 310, 288, 263, 229, 198, 150, 89, and 49 mA h g^{-1}, respectively. This inferior performance is mainly due to the absence of an rGO framework, which otherwise enhances charge transport and redox kinetics. Furthermore, when the current density was reverted to 0.1 A g^{-1}, the (Co,Mo)Se/rGO@PDA-NC anode recovered a discharge capacity of 383 mA h g^{-1}, demonstrating excellent capacity retention and highlighting the structural superiority and rapid Na-ion diffusion capability of the optimized nanostructure.

To further explore the reaction kinetics for three anodes, the prepared anodes were analyzed using CV results obtained at various voltage scan rates ranging from 0.1 to 2.0 mV s^{-1}, as presented in Fig. 5a, Fig. S13a, and S13b. Notably, the CV curve shapes remained largely unchanged even at a high scan rate of 2.0 mV s^{-1}, suggesting comparable reaction kinetics across all prepared anodes. It is important to highlight that the CV curves reflect a combination of capacitive-controlled and diffusion-controlled processes, which were separately analyzed to gain deeper insights into the reaction dynamics. The relationship between the peak current (i) and the scan rate (ν) was examined using the power law equations [75]:

$$i = a\nu^{b} \tag{9}$$

$$\log(i) = \log(a) + b\log(\nu) \tag{10}$$

where i and ν are variables, while a and b are constants determined from the intercept and slope of the log-log plot. Notably, a b-value close to 0.5 indicates a diffusion-controlled mechanism, while a b-value approaching 1 suggests a capacitive-dominated process [76]. The b-values for the anodic and cathodic peaks of the (Co,Mo)Se/rGO@PDA-NC, (Co,Mo)Se@PDA-NC, and CoSe/rGO@PDA-NC anodes are presented in Fig. 5b, Fig. S13c, and S13d. For (Co,Mo)Se/rGO@PDA-NC, the b-values for various redox peaks are close to 1 (e.g., 0.85, 0.92, 0.86, 0.85, and 0.88), implying a predominantly capacitive-controlled mechanism. Similarly, the b-values for CoSe/rGO@PDA-NC anode (Fig. S13d) are nearly comparable, indicating a similar capacitive contribution. Meanwhile, (Co,Mo)Se@PDA-NC anode (Fig. S13c) exhibits slightly lower b-values, suggesting a relatively reduced pseudocapacitive contribution compared to (Co,Mo)Se/rGO@PDA-NC anode. This trend highlights the role of rGO in enhancing charge storage kinetics. Furthermore, to gain deeper insight into the pseudocapacitive contribution, the CV curves were quantitatively analyzed using the following equation [42]:

$$i = k_1\nu + k_2\nu^{1/2} \tag{11}$$

where the first term corresponds to the capacitive-controlled contribution and the second term represents the diffusion-controlled contribution [77]. The constants k_1 and k_2 were determined from the slope and intercept of the $i(V)/\nu^{1/2}$ versus $\nu^{1/2}$ plot. As shown in Fig. 5c, the (Co,Mo)Se/rGO@PDA-NC anode demonstrates a capacitive contribution factor ($k_1\nu$) of 88 % at a scan rate of 2.0 mV s^{-1}. Besides, the anode consistently displays high capacitive contribution of 62, 70, 76, 81, and 85 % at 0.1, 0.4, 0.8, 1.2, and 1.6 mV s^{-1}, respectively (Fig. 5d). Likewise, the (Co,Mo)Se@PDA-NC (Fig. 5e and f) and CoSe/rGO@PDA-NC (Fig. 5g and h) anodes show comparable percentages of capacitive processes, reaching 59/70 %, 67/77 %, 74/81 %, 79/85 %, 83/88 %, and 87/91 %, respectively, at identical voltage scan rates. The slightly higher capacitive contribution of the CoSe/rGO@PDA-NC anode is primarily due to its loosely packed structure compared to the other two samples, which facilitates better electrolyte penetration and increases the proportion of surface-driven redox reactions, leading to a greater pseudocapacitive effect. This is further supported by BET analysis, where CoSe/rGO@PDA-NC and (Co,Mo)Se/rGO@PDA-NC anodes exhibit surface areas of 38 and 15 m^2 g^{-1}, respectively, with the higher surface area of CoSe/rGO@PDA-NC anode contributing to its greater pseudocapacitive effect.

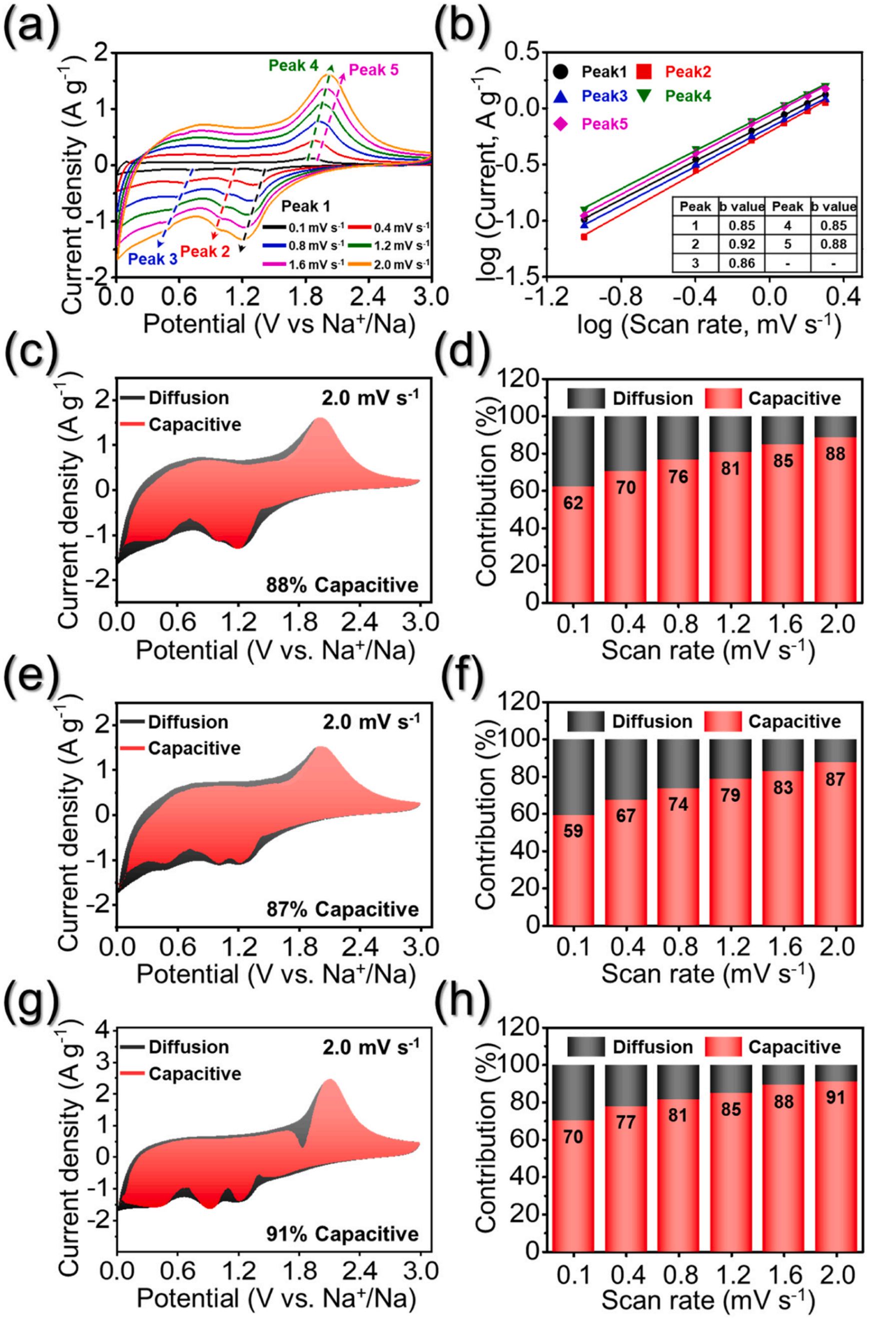

Fig. 5. Electrochemical reaction dynamics analysis of (a–d) (Co,Mo)Se/rGO@PDA-NC, (e, f) (Co,Mo)Se@PDA-NC, (g, h) CoSe/rGO@PDA-NC anodes: (a) CV curves obtained at various scan rates, (b) current response (*i*) *vs.* scan rate (*n*) at each redox peak, (c, e, g) CV curves with the capacitive fraction shown by the red region at a scan rate of 2.0 mV s^{-1}, and (d, f, h) bar chart showing the percentage of the capacitive contribution at different scan rates.

EIS measurements were performed to investigate the charge transfer kinetics of the different anodes at various cycling stages, including the fresh state, after the 1st cycle, and after the 300th cycle at current density of 1.0 A g^{-1}. The corresponding Nyquist plots are presented in Fig. 6a–c, while the fitted parameters, obtained using a Randles-type equivalent circuit (Fig. S14), are summarized in Table S3. The Nyquist plots of the fresh cells (Fig. 6a) reveal similar electrolyte resistance (R_s) of approximately 20 Ω for all anodes, indicating identical electrode-electrolyte interfacial conditions. However, the charge transfer resistance (R_{ct}) varies significantly, with (Co,Mo)Se/rGO@PDA-NC exhibiting the lowest R_{ct} (698 Ω), followed by (Co,Mo)Se@PDA-NC (790 Ω) and CoSe/rGO@PDA-NC anodes (882 Ω). The relatively higher R_{ct} of CoSe/rGO@PDA-NC is attributed to its sparse morphology, which increases electrolyte exposure but reduces charge transfer efficiency. Meanwhile, the larger R_{ct} observed for (Co,Mo)Se@PDA-NC than (Co,Mo)Se/rGO@PDA-NC anode is due to the absence of the highly conductive rGO framework, which otherwise facilitates charge transport. Furthermore, after the 1st cycle, the R_{ct} values decrease significantly for all anodes, with the most pronounced reduction observed in (Co,Mo)Se/rGO@PDA-NC (105 Ω), followed by CoSe/rGO@PDA-NC (137 Ω) and (Co,Mo)Se@PDA-NC anodes (142 Ω) (Fig. 6b). This substantial decrease is attributed to the formation of ultrafine amorphous-like (Co,Mo)Se nanocrystals and the development of a stable SEI layer, which facilitates charge transfer [54]. After 300 cycles (Fig. 6c), the (Co,Mo)Se/rGO@PDA-NC anode maintains the lowest R_{ct} value (70 Ω), demonstrating superior charge transfer kinetics compared to (Co,Mo)Se@PDA-NC (82 Ω) and CoSe/rGO@PDA-NC anodes (236 Ω). The substantial increase in R_{ct} for CoSe/rGO@PDA-NC anode aligns with its

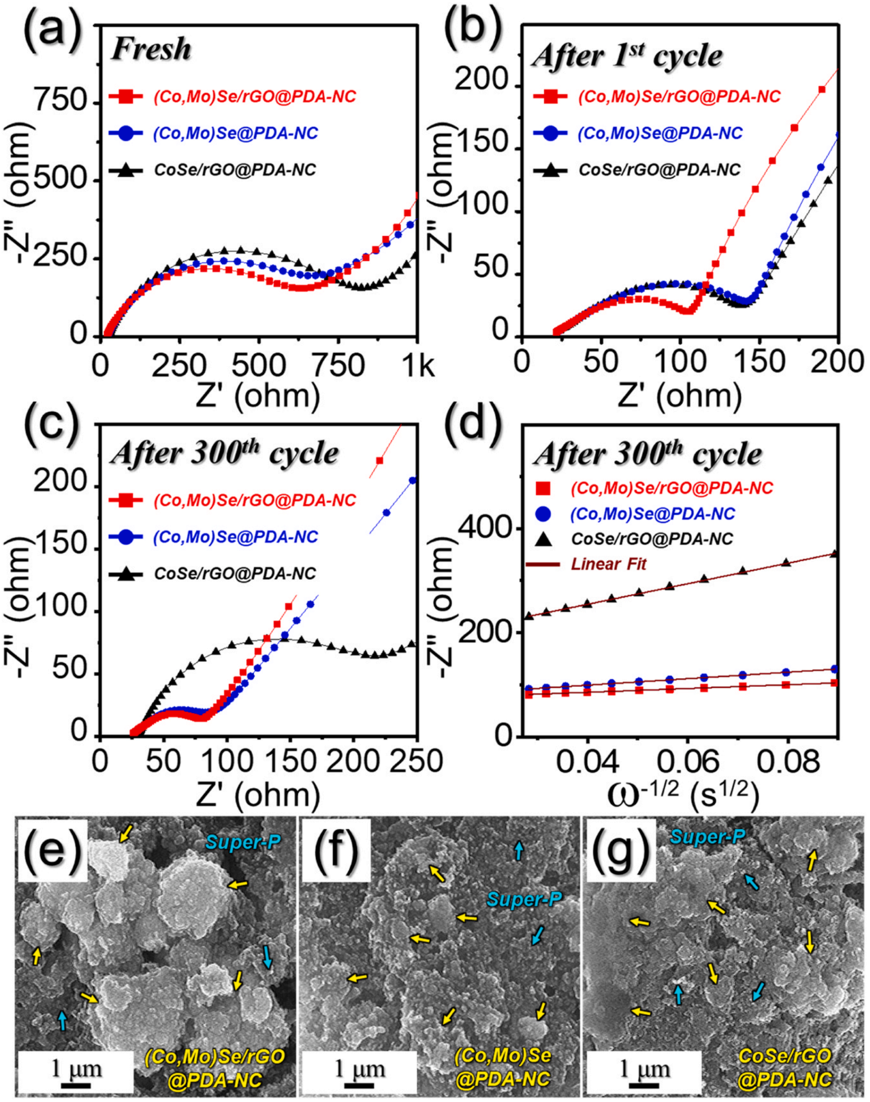

Fig. 6. (a–c) Nyquist impedance plots of (Co,Mo)Se/rGO@PDA-NC, (Co,Mo)Se@PDA-NC, CoSe/rGO@PDA-NC anodes: (a) before cycling, (b) after 1st cycle, (c) after 300th cycle; (d) relationships between the real part of the impedance (Z_{re}) and $\omega^{-1/2}$ obtained after 300 cycles at 1.0 A g^{-1}, and FE-SEM images of the (e) (Co,Mo)Se/rGO@PDA-NC, (f) (Co,Mo)Se@PDA-NC, and (g) CoSe/rGO@PDA-NC microspheres obtained after 300 cycles at 1.0 A g.$^{-1}$

structural pulverization, as reflected in its cycling performance (Fig. 4d), indicating severe degradation of charge transfer pathways. Furthermore, the Na-ion diffusion coefficients (D_{Na^+}) were calculated using the Warburg impedance factor (σ_w) derived from the relationship $Z' = R_s + R_{ct} + \sigma_w \omega^{-1/2}$ (Fig. 6d) [78]. The (Co,Mo)Se/rGO@PDA-NC anode exhibits the least steep slope, indicating higher D_{Na^+} due to its highly conductive nanostructure. The D_{Na^+} was calculated using the following equation [79]:

$$D = 0.5R^2T^2/A^2F^4C^2\sigma_w^2 \tag{12}$$

Here, R denotes the gas constant, T is the temperature, A represents the electrode area, C is the concentration of lithium ions, F stands for the Faraday constant, and σ_w corresponds to the Warburg impedance factor. The (Co,Mo)Se/rGO@PDA-NC anode exhibits the highest D_{Na^+} (1.14×10^{-13} cm^2 s^{-1}), which is an order of magnitude higher than that of (Co,Mo)Se@PDA-NC (3.90×10^{-14} cm^2 s^{-1}) and two orders of magnitude higher than CoSe/rGO@PDA-NC (3.85×10^{-15} cm^2 s^{-1}). This enhanced Na-ion diffusion efficiency further supports the superior redox reaction kinetics of the (Co,Mo)Se/rGO@PDA-NC anode, facilitated by its highly conductive NGC/rGO network, PDA-NC coating, and interfacial synergy between $Co_{0.85}Se$ and $MoSe_2$ nanocrystals. Notably, the obtained D_{Na^+} of the (Co,Mo)Se/rGO@PDA-NC anode is significantly higher than those of previously reported Co- and Mo-based selenide anodes for SIBs, as summarized in Table S4. This is attributed to the synergistic effects of the hierarchical conductive framework and the well-engineered bimetallic heterointerface, which together facilitate rapid ion transport and redox kinetics. In particular, the heterointerface between conductive $Co_{0.85}Se$ (NiAs-type structure) and semiconducting $MoSe_2$ (2 H phase) plays a crucial role in promoting both electron/ion transport. Owing to the difference in electronic structures and work functions, a built-in internal electric field is established at the interface, which facilitates charge redistribution and accelerates both electron transfer and Na-ion migration across the junction [80,81]. This interfacial effect, combined with the high conductivity of $Co_{0.85}Se$ and the layered Na-ion diffusion channels of $MoSe_2$, enhances redox kinetics and suppresses polarization during cycling [82,83]. Simultaneously, the interconnected NGC/rGO framework provides continuous electron pathways and mechanical support, further contributing to rapid charge transport and structural robustness under electrochemical stress [84,85]. Furthermore, post-cycling morphological analysis (Fig. 6e–g) was conducted to evaluate the structural integrity of the anodes after prolonged cycling. The (Co,Mo)Se/rGO@PDA-NC anode (Fig. 6e) successfully retained its spherical morphology, demonstrating excellent structural stability. This robust architecture is primarily attributed to the rGO framework, which acts as a self-supporting skeleton, effectively mitigating the mechanical stress induced by volume fluctuations. In contrast, the (Co,Mo)Se@PDA-NC anode (Fig. 6 f) exhibited severe structural degradation, with its spherical morphology collapsing into aggregated and fragmented particles due to the absence of an rGO framework, which otherwise reinforces mechanical stability. Meanwhile, the CoSe/rGO@PDA-NC anode (Fig. 6 g) suffered the most severe pulverization, with the nanostructure not only breaking apart but also being covered with thick layers of byproducts from undesired side reactions during cycling. Despite the presence of rGO frameworks, the absence of uniform hybridization and structural densification induced by Mo-species led to a porous architecture that failed to maintain structural integrity during long-term cycling. These observations corroborate the electrochemical cycling performance trends, confirming that the superior cycling stability of (Co,Mo)Se/rGO@PDA-NC is directly linked to its structurally robust design. The combination of rGO-enhanced conductivity, Co–Mo hybridization, and the stabilizing PDA-NC layer collectively contributes to its exceptional electrochemical performance, prolonged cycling durability, and improved rate capability.

4. Conclusions

In summary, PDA-NC-coated composite microspheres, incorporating a rGO framework embedded with bimetallic $Co_{0.85}Se/MoSe_2$ nanocrystals ((Co,Mo)Se/rGO@PDA-NC microspheres), were successfully synthesized through a facile and scalable spray drying process, followed by controlled selenization and surface coating procedures. The hierarchical nanostructure was precisely designed to overcome the limitations of conventional metal selenide-based anodes. The MOF-derived CoMo-LDH precursor facilitated the homogeneous atomic-level hybridization of Co and Mo, leading to the uniform formation of $Co_{0.85}Se/MoSe_2$ nanocrystals during selenization while mitigating phase segregation. The self-supporting rGO and NGC framework provided an electron transport network and enhanced structural stability, effectively maintaining the integrity of the MOF-derived components during heat treatment and electrochemical cycling. Additionally, the PDA-NC layer acted as an interconnecting bridge between microspheres, enabling continuous charge carrier transport and reducing mechanical degradation caused by volume fluctuations. As a result, the (Co,Mo)Se/rGO@PDA-NC anode exhibited superior electrochemical performance, including a high rate capability of up to 7.0 A g^{-1} and extended cycling stability over 300 cycles at 1.0 A g^{-1}. Furthermore, the optimized nanostructure enhanced charge transport kinetics, leading to an improved Na-ion diffusion coefficient of approximately 10^{-13} cm^2 s^{-1}. The comprehensive physicochemical and electrochemical analyses in this study provided valuable insights into the rational design of multi-component metal selenide-based hybrid anodes. These findings demonstrated the potential of structurally robust and highly conductive nanostructures for next-generation SIBs and other advanced energy storage applications.

CRediT authorship contribution statement

CHO JUNG SANG: Writing – review & editing, Supervision, Project administration, Funding acquisition, Conceptualization. **Chungyeon Cho:** Writing – review & editing, Project administration, Methodology, Conceptualization. **Gi Dae Park:** Writing – original draft, Supervision, Formal analysis, Conceptualization. **Sung Woo Cho:** Writing – original draft, Visualization, Software, Investigation. **Rakesh Saroha:** Writing – review & editing, Visualization, Investigation, Data curation. **Dong Guk Ryu:** Writing – original draft, Visualization, Validation, Resources, Conceptualization. **Jae Seob Lee:** Writing – original draft, Visualization, Resources, Investigation, Conceptualization.

Declaration of Competing Interest

The authors declare that they have no known competing financial interests or personal relationships that could have appeared to influence the work reported in this paper.

Acknowledgments

This work was supported by the National Research Foundation of Korea (NRF) grant funded by the Korea government (MSIT) (Grant no.: RS-2023-00217581, RS-2025-00556955). This work was supported by Chungbuk National University NUDP program (2024).

Appendix A. Supporting information

Supplementary data associated with this article can be found in the online version at doi:10.1016/j.jallcom.2025.182406.

References

[1] H.W. Kim, J. Han, Characterization of the Ge@GeO_2-C composite anode synthesized using a simple high-energy ball-milling process for Li-ion batteries, Korean J. Chem. Eng. 41 (2024) 3019–3026, https://doi.org/10.1007/s11814-024-00245-8.

[2] U. Kulkarni, W.-J. Cho, S.-K. Cho, J.-J. Hong, K.P. Shejale, G.-R. Yi, Solid polymer electrolytes-based composite cathodes for advanced solid-state lithium batteries, Korean J. Chem. Eng. 41 (2024) 385–402, https://doi.org/10.1007/s11814-024-00122-4.

[3] I.T. Bello, L.A. Jolaoso, R.A. Ahmed, A. Bello, Electrochemical energy conversion and storage systems: a perspective on the challenges and opportunities for sustainable energy in Africa, Energy Rev. 4 (1) (2024) 100109, https://doi.org/10.1016/j.enrev.2024.100109.

[4] E. Fan, L. Li, Z. Wang, J. Lin, Y. Huang, Y. Yao, R. Chen, F. Wu, Sustainable recycling technology for Li-ion batteries and beyond: challenges and future prospects, Chem. Rev. 120 (14) (2020) 7020–7063, https://doi.org/10.1021/acs.chemrev.9b00535.

[5] P. Yadav, V. Shelke, A. Patrike, M. Shelke, Sodium-based batteries: development, commercialization journey and new emerging chemistries, Oxf. Open Mater. Sci. 3 (1) (2023) itac019, https://doi.org/10.1093/oxfmat/itac019.

[6] L. Zhao, T. Zhang, H. Zhao, Y. Hou, Polyanion-type electrode materials for advanced sodium-ion batteries, Mater. Today Nano 10 (2020) 100072, https://doi.org/10.1016/j.mtnano.2020.100072.

[7] W. Lee, J. Kim, S. Yun, W. Choi, H. Kim, W.-S. Yoon, Multiscale factors in designing alkali-ion (Li, Na, and K) transition metal inorganic compounds for next-generation rechargeable batteries, Energy Environ. Sci. 13 (12) (2020) 4406–4449, https://doi.org/10.1039/D0EE01277G.

[8] H. Zhang, L. Wang, P. Zuo, Advances in sodium-ion battery cathode materials: exploring chemistry, reaction mechanisms, and prospects for next-generation energy storage systems, J. Mater. Chem. A 12 (45) (2024) 30971–31003, https://doi.org/10.1039/D4TA03748K.

[9] Z. Tang, S. Zhou, Y. Huang, H. Wang, R. Zhang, Q. Wang, D. Sun, Y. Tang, H. Wang, Improving the initial coulombic efficiency of carbonaceous materials for Li/Na-ion batteries: origins, solutions, and perspectives, Electrochem. Energy Rev. 6 (1) (2023) 8, https://doi.org/10.1007/s41918-022-00178-y.

[10] T. Bashir, S. Zhou, S. Yang, S.A. Ismail, T. Ali, H. Wang, J. Zhao, L. Gao, Progress in 3D-MXene electrodes for lithium/sodium/potassium/magnesium/zinc/aluminum-ion batteries, Electrochem. Energy Rev. 6 (1) (2023) 5, https://doi.org/10.1007/s41918-022-00174-2.

[11] H. Chaudhuri, Y.-S. Yun, A critical review on the properties and energy storage applications of graphene oxide/layered double hydroxides and graphene oxide/MXenes, J. Power Sources 564 (2023) 232870, https://doi.org/10.1016/j.jpowsour.2023.232870.

[12] T. Hu, Z. Gu, G.R. Williams, M. Strimaite, J. Zha, Z. Zhou, X. Zhang, C. Tan, R. Liang, Layered double hydroxide-based nanomaterials for biomedical applications, Chem. Soc. Rev. 51 (14) (2022) 6126–6176, https://doi.org/10.1039/D2CS00236A.

[13] M. Sarfraz, I. Shakir, Recent advances in layered double hydroxides as electrode materials for high-performance electrochemical energy storage devices, J. Energy Storage 13 (2017) 103–122, https://doi.org/10.1016/j.est.2017.06.011.

[14] R.K. Kankala, Nanoarchitectured two-dimensional layered double hydroxides-based nanocomposites for biomedical applications, Adv. Drug Deliv. Rev. 186 (2022) 114270, https://doi.org/10.1016/j.addr.2022.114270.

[15] X. Long, Z. Wang, S. Xiao, Y. An, S. Yang, Transition metal based layered double hydroxides tailored for energy conversion and storage, Mater. Today 19 (4) (2016) 213–226, https://doi.org/10.1016/j.mattod.2015.10.006.

[16] H. Yin, Z. Tang, Ultrathin two-dimensional layered metal hydroxides: an emerging platform for advanced catalysis, energy conversion and storage, Chem. Soc. Rev. 45 (18) (2016) 4873–4891, https://doi.org/10.1039/C6CS00343E.

[17] J. Chu, Y. Wang, F. Zhong, X. Feng, W. Chen, X. Ai, H. Yang, Y. Cao, Metal/covalent-organic frameworks for electrochemical energy storage applications, EcoMat 3 (5) (2021) e12133, https://doi.org/10.1002/eom2.12133.

[18] M. Jafari, F. Ganjali, R. Eivazzadeh-Keihan, A. Maleki, S. Geranmayeh, Recent advances in applications of graphene-layered double hydroxide nanocomposites in supercapacitors and batteries, FlatChem 45 (2024) 100658, https://doi.org/10.1016/j.flatc.2024.100658.

[19] Z. Liang, R. Zhao, T. Qiu, R. Zou, Q. Xu, Metal-organic framework-derived materials for electrochemical energy applications, EnergyChem 1 (1) (2019) 100001, https://doi.org/10.1016/j.enchem.2019.100001.

[20] M.H. Lee, S. Lee, K.S. Yoo, Synthesis of Fe–MOF/COF hybrid materials for methane adsorption using design of experiments, Korean J. Chem. Eng. 41 (2024) 435–444, https://doi.org/10.1007/s11814-024-00015-6.

[21] Z. Yin, Y.-L. Zhou, M.-H. Zeng, M. Kurmoo, The concept of mixed organic ligands in metal–organic frameworks: design, tuning and functions, Dalton Trans. 44 (12) (2015) 5258–5275, https://doi.org/10.1039/C4DT04030A.

[22] Y. Yang, S. Ma, M. Xia, Y. Guo, Y. Zhang, L. Liu, C. Zhou, G. Chen, X. Wang, Q. Wu, Elaborately converting hierarchical NiCo–LDH to rod–like LDH–decorated MOF as interlayer for high–performance lithium–sulfur battery, Mater. Today Phy. 35 (2023) 101112, https://doi.org/10.1016/j.mtphys.2023.101112.

[23] N. Zhang, S.-X. Guan, Q. Zhang, J.-R. Zhao, J.-Y. Zhang, Q.-F. Ke, Y.-Z. Fang, The space-charge region at NiFe-MOF⊆LDH pn junction by self-sacrificing LDH to boost oxygen evolution tandem with in-situ electro-Fenton, Chem. Eng. J. 473 (2023) 145223, https://doi.org/10.1016/j.cej.2023.145223.

[24] L. Zhu, T. Han, Y. Ding, J. Long, X. Lin, J. Liu, A metal–organic-framework derived $NiFe_2O_4$@NiCo-LDH nanocube as high-performance lithium-ion battery anode under different temperatures, Appl. Surf. Sci. 599 (2022) 153953, https://doi.org/10.1016/j.apsusc.2022.153953.

[25] J.S. Lee, R. Saroha, J.S. Cho, Porous microspheres comprising $CoSe_2$ nanorods coated with N-doped graphitic C and polydopamine-derived C as anodes for long-lived Na-ion batteries, NanoMicro Lett. 14 (1) (2022) 113, https://doi.org/10.1007/s40820-022-00855-z.

[26] Y. Huang, Z. Wang, Y. Jiang, S. Li, Z. Li, H. Zhang, F. Wu, M. Xie, L. Li, R. Chen, Hierarchical porous $Co_{0.85}Se$@reduced graphene oxide ultrathin nanosheets with vacancy-enhanced kinetics as superior anodes for sodium-ion batteries, Nano Energy 53 (2018) 524–535, https://doi.org/10.1016/j.nanoen.2018.09.010.

[27] Y. Xu, X. Liu, H. Su, S. Jiang, J. Zhang, D. Li, Hierarchical bimetallic selenides $CoSe_2$–$MoSe_2$/rGO for sodium/potassium-ion batteries anode: insights into the intercalation and conversion mechanism, Energy Environ. Mater. 5 (2022) 627–636, https://doi.org/10.1002/eem2.12206.

[28] Q. Lin, Z. Yuan, D. Wang, W. Wei, X. Wang, W. Han, L. Wang, Co-Co LDH-derived $CoSe_2$ anchored on N-doped carbon nanospheres as high-performance anodes for sodium-ion batteries, Electrochim. Acta 432 (2022) 141012, https://doi.org/10.1016/j.electacta.2022.141012.

[29] J. Wang, X. Yue, X. Cao, Z. Liu, A.M. Patil, J. Wang, X. Hao, A. Abudula, G. Guan, Metal organic frameworks derived CoS_2/NiS_2 heterostructure toward high-performance sodium storage anode materials, Chem. Eng. J. 431 (Part 2) (2022) 134091, https://doi.org/10.1016/j.cej.2021.134091.

[30] S. Wu, X. Li, Y. Zhang, H. Fan, Selenium (Se) doped $CoS_{2\text{-}x}Se_x$/NC laminated nanosheets assembled accordion architecture for robust and durable sodium/potassium ion batteries, Chem. Eng. Sci. 313 (2025) 121737, https://doi.org/10.1016/j.ces.2025.121737.

[31] S. Lu, J. Lin, C. Wang, Y. Zhang, Y. Zhang, H. Fan, Heterogeneous engineering of MnSe@NC@ReS_2 core-shell nanowires for advanced sodium-/potassium-ion batteries, Rare Met 43 (8) (2024) 3713–3723, https://doi.org/10.1007/s12598-024-02650-8.

[32] Z. Qin, P. Xia, X. Liu, X. Jin, S. Lu, Y. Zhang, H. Fan, Recycling graphite from waste lithium-ion batteries for carbon dots@graphite (CDs@Gra) hybrid as advanced potassium ion battery anode, J. Energy Storage 121 (2025) 116628, https://doi.org/10.1016/j.est.2025.116628.

[33] M. Kim, J.H. Kim, Y.C. Kang, Solution-phase selenization engineering of zeolitic imidazolate framework (ZIF)-67-derived $Co_{0.85}Se$@nitrogen-doped carbon for potassium-ion storage, Appl. Surf. Sci. 614 (2023) 156218, https://doi.org/10.1016/j.apsusc.2022.156218.

[34] M.S. Jo, S. Ghosh, S.M. Jeong, Y.C. Kang, J.S. Cho, Coral-like yolk–shell-structured nickel oxide/carbon composite microspheres for high-performance Li-ion storage anodes, NanoMicro Lett. 11 (2019) 1–18, https://doi.org/10.1007/s40820-018-0234-0.

[35] F. Wang, H. Guo, Y. Chai, Y. Li, C. Liu, The controlled regulation of morphology and size of HKUST-1 by "coordination modulation method, Microporous Mesoporous Mater. 173 (2013) 181–188, https://doi.org/10.1016/j.micromeso.2013.02.023.

[36] S. Sundriyal, V. Shrivastav, H. Kaur, S. Mishra, A. Deep, High-performance symmetrical supercapacitor with a combination of a ZIF-67/rGO composite electrode and a redox additive electrolyte, ACS Omega 3 (12) (2018) 17348–17358, https://doi.org/10.1021/acsomega.8b02065.

[37] C. Wu, D. Liu, H. Li, J. Li, Molybdenum carbide-decorated metallic cobalt@nitrogen-doped carbon polyhedrons for enhanced electrocatalytic hydrogen evolution, Small 14 (16) (2018) 1704227, https://doi.org/10.1002/smll.201704227.

[38] X. Zhao, H. Xu, Z. Hui, Y. Sun, C. Yu, J. Xue, R. Zhou, L. Wang, H. Dai, Y. Zhao, Electrostatically assembling 2D nanosheets of MXene and MOF-derivatives into 3D hollow frameworks for enhanced lithium storage, Small 15 (47) (2019) 1904255, https://doi.org/10.1002/smll.201904255.

[39] J. Bao, Z. Wang, J. Xie, L. Xu, F. Lei, M. Guan, Y. Huang, Y. Zhao, J. Xia, H. Li, The CoMo-LDH ultrathin nanosheet as a highly active and bifunctional electrocatalyst for overall water splitting, Inorg. Chem. Front 5 (11) (2018) 2964–2970, https://doi.org/10.1039/C8QI00867A.

[40] F.J. Maldonado-Hódar, C. Moreno-Castilla, J. Rivera-Utrilla, Y. Hanzawa, Y. Yamada, Catalytic graphitization of carbon aerogels by transition metals, Langmuir 16 (2000) 4367–4373, https://doi.org/10.1021/la991080r.

[41] A. Ōya, S. Ōtani, Catalytic graphitization of carbons by various metals, Carbon 17 (1979) 131–137, https://doi.org/10.1016/0008-6223(79)90020-4.

[42] J.S. Lee, J.-S. Park, K.W. Baek, R. Saroha, S.H. Yang, Y.C. Kang, J.S. Cho, Coral-like porous microspheres comprising polydopamine-derived N-doped C-coated $MoSe_2$ nanosheets composited with graphitic carbon as anodes for high-rate sodium-and potassium-ion batteries, Chem. Eng. J. 456 (2023) 141118, https://doi.org/10.1016/j.cej.2022.141118.

[43] S. Meng, Q. Nie, W. Yaseen, H. Mao, M. Xie, M. Chen, J. Xie, Y. Xu, One-step fabrication of hierarchically flower-like N-doped carbon-CoMo-LDH nanosheets for efficient overall alkaline water splitting, Int. J. Hydrog. Energy 99 (2025) 93–101, https://doi.org/10.1016/j.ijhydene.2024.12.116.

[44] R. Saroha, H.S. Ka, G.D. Park, C. Cho, D.-W. Kang, J.S. Cho, Long-term stability of lithium–sulfur batteries via synergistic integration of nitrogen-doped graphitic carbon-coated cobalt selenide nanocrystals within porous three-dimensional graphene-carbon nanotube microspheres, J. Power Sources 592 (2024) 233893, https://doi.org/10.1016/j.jpowsour.2023.233893.

[45] R. Saroha, J.H. Oh, J.S. Lee, Y.C. Kang, S.M. Jeong, D.-W. Kang, C. Cho, J.S. Cho, Hierarchically porous nanofibers comprising multiple core–shell Co_3O_4@ graphitic carbon nanoparticles grafted within N-doped CNTs as functional interlayers for excellent Li–S batteries, Chem. Eng. J. 426 (2021) 130805, https://doi.org/10.1016/j.cej.2021.130805.

[46] M.J. Matthews, M.A. Pimenta, G. Dresselhaus, M. Dresselhaus, M. Endo, Origin of dispersive effects of the Raman D band in carbon materials, Phy. Rev. B 59 (10) (1999) R6585, https://doi.org/10.1103/PhysRevB.59.R6585.

[47] J. Paredes, S. Villar-Rodil, P. Solís-Fernández, A. Martínez-Alonso, J. Tascon, Atomic force and scanning tunneling microscopy imaging of graphene nanosheets derived from graphite oxide, Langmuir 25 (10) (2009) 5957–5968, https://doi.org/10.1021/la804216z.

[48] L. Li, Q. Yuan, S. Ye, Y. Fu, X. Ren, Q. Zhang, J. Liu, *In situ* formed lithium ionic conductor thin film on the surface of high-crystal-layered $LiCoO_2$ as a high-voltage cathode material, Mater. Chem. Front 5 (16) (2021) 6171–6181, https://doi.org/10.1039/D1QM00627D.

[49] R. Saroha, Y.H. Seon, B. Jin, Y.C. Kang, D.-W. Kang, S.M. Jeong, J.S. Cho, Self-supported hierarchically porous 3D carbon nanofiber network comprising Ni/Co/$NiCo_2O_4$ nanocrystals and hollow N-doped C nanocages as sulfur host for highly reversible Li–S batteries, Chem. Eng. J. 446 (2022) 137141, https://doi.org/10.1016/j.cej.2022.137141.

[50] Y. Sun, C. Li, S. Jiang, R. Xia, X. Wang, H. Bao, M. Gao, Comparative study on supercapacitive and oxygen evolution reaction applications of hollow nanostructured cobalt sulfides, Nanotechnol 32 (38) (2021) 385401, https://doi.org/10.1088/1361-6528/ac09aa.

[51] L. Zhang, J. Zhu, Z. Wang, W. Zhang, 2D $MoSe_2$/CoP intercalated nanosheets for efficient electrocatalytic hydrogen production, Int. J. Hydrog. Energy 45 (38) (2020) 19246–19256, https://doi.org/10.1016/j.ijhydene.2020.05.059.

[52] C. Li, A. Wang, L. Wu, X. He, J. Zhang, X. Hao, L. Feng, Properties of $CdSe_{1-x}S_x$ films by magnetron sputtering and their role in CdTe solar cells, J. Mater. Sci. Mater. Electron 31 (2020) 21455–21466, https://doi.org/10.1007/s10854-020-04659-y.

[53] Q.-S. Jiang, W. Li, J. Wu, W. Cheng, J. Zhu, Z. Yan, X. Wang, Y. Ju, Electrodeposited cobalt and nickel selenides as high-performance electrocatalytic materials for dye-sensitized solar cells, J. Mater. Sci. Mater. Electron 30 (2019) 9429–9437, https://doi.org/10.1007/s10854-019-01273-5.

[54] C.S. Kim, R. Saroha, H.H. Choi, J.H. Oh, G.D. Park, D.-W. Kang, J.S. Cho, High-performance cathode promoted by reduced graphene oxide nanofibers with well-defined interconnected meso-/micro pores for rechargeable Li-Se batteries, J. Ind. Eng. Chem. 121 (2023) 489–498, https://doi.org/10.1016/j.jiec.2023.02.004.

[55] A.V. Ramya, R. Thomas, M. Balachandran, Mesoporous onion-like carbon nanostructures from natural oil for high-performance supercapacitor and electrochemical sensing applications: Insights into the post-synthesis sonochemical treatment on the electrochemical performance, Ultrason. Sonochem. 79 (2021) 105767, https://doi.org/10.1016/j.ultsonch.2021.105767.

[56] R. Saroha, D.Y. Shin, J.S. Lee, S.W. Cho, D.-H. Lim, J.S. Cho, Theoretically endured defect-engineered antimony selenide nanocrystals grafted within three-dimensional reduced graphene oxide hollow microspheres with large open cavities as polysulfide barrier for robust sulfur kinetics, Adv. Compos. Hybrid. Mater. 7 (2024) 93, https://doi.org/10.1007/s42114-024-00892-9.

[57] J.Y. Lee, N.Y. Kim, D.Y. Shin, H.-Y. Park, S.-S. Lee, S. Joon Kwon, D.-H. Lim, K. W. Bong, J.G. Son, J.Y. Kim, Nitrogen-doped graphene-wrapped iron nanofragments for high-performance oxygen reduction electrocatalysts, J. Nanopart. Res. 19 (2017) 98, https://doi.org/10.1007/s11051-017-3793-y.

[58] S. Ravi, S. Zhang, Y.-R. Lee, K.-K. Kang, J.-M. Kim, J.-W. Ahn, W.-S. Ahn, EDTA-functionalized KCC-1 and KIT-6 mesoporous silicas for Nd^{3+} ion recovery from aqueous solutions, J. Ind. Eng. Chem. 67 (2018) 210–218, https://doi.org/10.1016/j.jiec.2018.06.031.

[59] J.C. Groen, L.A.A. Peffer, J. Pérez-Ramírez, Pore size determination in modified micro- and mesoporous materials. Pitfalls and limitations in gas adsorption data analysis, Microporous Mesoporous Mater. 60 (1–3) (2003) 1, https://doi.org/10.1016/S1387-1811(03)00339-1.

[60] M. Jiang, Y. Hu, B. Mao, Y. Wang, Z. Yang, T. Meng, X. Wang, M. Cao, Strain-regulated Gibbs free energy enables reversible redox chemistry of chalcogenides

for sodium ion batteries, Nat. Commun. 13 (2022) 5588, https://doi.org/10.1038/s41467-022-33329-2.
[61] M. Liu, P. Jing, T. Wang, X. Hou, M. Liu, Z. Sun, J. Li, D. He, Pseudocapacitive reaction enhanced porous $Co_{0.85}Se$/N-doped carbon anodes for advanced sodium-ion battery with high rate and capacity, Electrochim. Acta 321 (2019) 134643, https://doi.org/10.1016/j.electacta.2019.134643.
[62] Y. Tang, Z. Zhao, Y. Wang, Y. Dong, Y. Liu, X. Wang, J. Qiu, Carbon-stabilized interlayer-expanded few-layer $MoSe_2$ nanosheets for sodium ion batteries with enhanced rate capability and cycling performance, ACS Appl. Mater. Interfaces 8 (47) (2016) 32324–32332, https://doi.org/10.1021/acsami.6b11230.
[63] G. Zhang, K. Liu, S. Liu, H. Song, J. Zhou, Flexible $Co_{0.85}Se$ nanosheets/graphene composite film as binder-free anode with high Li-and Na-Ion storage performance, J. Alloy. Compd. 731 (2018) 714–722, https://doi.org/10.1016/j.jallcom.2017.10.094.
[64] J. Li, Y. He, Y. Dai, H. Zhang, Y. Zhang, S. Gu, X. Wang, T. Gao, G. Zhou, L. Xu, Heterostructure interface construction of cobalt/molybdenum selenides toward ultra-stable sodium-ion half/full batteries, Adv. Funct. Mater. 34 (42) (2024) 2406915, https://doi.org/10.1002/adfm.202406915.
[65] Y. Cao, L. Xiao, M.L. Sushko, W. Wang, B. Schwenzer, J. Xiao, Z. Nie, L.V. Saraf, Z. Yang, J. Liu, Sodium ion insertion in hollow carbon nanowires for battery applications, Nano Lett. 12 (7) (2012) 3783–3787, https://doi.org/10.1021/nl3016957.
[66] Hg Wang, Z. Wu, Fl Meng, Dl Ma, Xl Huang, Lm Wang, Xb Zhang, Nitrogen-doped porous carbon nanosheets as low-cost, high-performance anode material for sodium-ion batteries, ChemSusChem 6 (1) (2013) 56–60, https://doi.org/10.1002/cssc.201200680.
[67] L. Ji, M. Gu, Y. Shao, X. Li, M.H. Engelhard, B.W. Arey, W. Wang, Z. Nie, J. Xiao, C. Wang, Controlling SEI formation on SnSb-porous carbon nanofibers for improved Na ion storage, Adv. Mater. 26 (18) (2014) 2901–2908, https://doi.org/10.1002/adma.201304962.
[68] P. Ge, C. Zhang, H. Hou, B. Wu, L. Zhou, S. Li, T. Wu, J. Hu, L. Mai, X. Ji, Anions induced evolution of Co_3X_4 (X = O, S, Se) as sodium-ion anodes: the influences of electronic structure, morphology, electrochemical property, Nano Energy 48 (2018) 617–629, https://doi.org/10.1016/j.nanoen.2018.04.018.
[69] B. Liu, J. Cao, J. Li, L. Li, D. Chen, S. Zhang, D. Cai, W. Han, Highly conductive Co_3Se_4 embedded in N-doped 3D interconnected carbonaceous network for enhanced lithium and sodium storage, J. Colloid Interface Sci. 586 (2021) 630–639, https://doi.org/10.1016/j.jcis.2020.10.131.
[70] J. Zhou, Y. Wang, J. Zhang, T. Chen, H. Song, H.Y. Yang, Two dimensional layered $Co_{0.85}Se$ nanosheets as a high-capacity anode for lithium-ion batteries, Nanoscale 8 (2016) 14992–15000, https://doi.org/10.1039/c6nr03571j.
[71] L. Shi, R. Liu, Y. Tang, J. Wang, Z. Wang, G. Cheng, M. Hu, Y. Yang, J. Ding, Fabrication of $Co_{0.85}Se$@CN double-walled hollow cages to address the volume expansion of anode and enhance ion diffusion for sodium-ion storage, Electrochim. Acta 426 (2022) 140839, https://doi.org/10.1016/j.electacta.2022.140839.
[72] J. Wang, X. Yue, X. Cao, Z. Liu, A.M. Patil, J. Wang, X. Hao, A. Abudula, G. Guan, Metal organic frameworks derived CoS_2/NiS_2 heterostructure toward high-performance sodium storage anode materials, Chem. Eng. J. 431 (2022) 134091, https://doi.org/10.1016/j.cej.2021.134091.
[73] X. Lin, R. Wang, W. Dong, F. Huang, Rational design of bimetallic oxide anodes for superior Li^+ storage, Acta Phys. Chim. Sin. 41 (2025) 100021, https://doi.org/10.3866/PKU.WHXB202311005.
[74] Y. Zhang, B. Han, S. Tan, Q. Gao, Z. Cai, C. Zhou, J. Li, R. Sun, K. Amine, Interfacial engineering of metal chalcogenides-based heterostructures for advanced sodium-ion batteries, Adv. Energy Mater. 15 (2025) 2404796, https://doi.org/10.1002/aenm.202404796.
[75] J.S. Lee, R. Saroha, J.H. Oh, C. Cho, B. Jin, D.-W. Kang, J.S. Cho, Camphene-derived hollow and porous nanofibers decorated with hollow NiO nanospheres and graphitic carbon as anodes for efficient lithium-ion storage, J. Ind. Eng. Chem. 114 (2022) 276–287, https://doi.org/10.1016/j.jiec.2022.07.017.
[76] J. Zhu, C. Shang, X. Wang, G. Zhou, Co_2P/Sn_4P_3 particle encapsulated in N, P codoped carbon nanocubes for efficient sodium storage, Mater. Today Chem. 19 (2021) 100389, https://doi.org/10.1016/j.mtchem.2020.100389.
[77] X. Xu, F. Li, D. Zhang, S. Ji, Y. Huo, J. Liu, Facile construction of $CoSn/Co_3Sn_2$@C nanocages as anode for superior lithium-/sodium-ion storage, Carbon Neutraliz 2 (1) (2023) 54–62, https://doi.org/10.1002/cnl2.40.
[78] R. Saroha, A.K. Panwar, Y. Sharma, P.K. Tyagi, S. Ghosh, Development of surface functionalized ZnO-doped $LiFePO_4$/C composites as alternative cathode material for lithium ion batteries, Appl. Surf. Sci. 394 (2017) 25–36, https://doi.org/10.1016/j.apsusc.2016.09.105.
[79] J. Pati, H. Raj, S.K. Sapra, A. Dhaka, A. Bera, S. Yusuf, R. Dhaka, Unraveling the diffusion kinetics of honeycomb structured $Na_2Ni_2TeO_6$ as a high-potential and stable electrode for sodium-ion batteries, J. Mater. Chem. A 10 (29) (2022) 15460–15473, https://doi.org/10.1039/D2TA01775J.
[80] L. Chen, Z. Liu, W. yang, S. Wu, Y. Li, Y. Zhang, L. Zeng, H. Fan, Micro-mesoporous cobalt phosphosulfide (Co_3S_4/CoP/NC) nanowires for ultrahigh rate capacity and ultrastable sodium ion battery, J. Colloid Interface Sci. 666 (2024) 416–423, https://doi.org/10.1016/j.jcis.2024.04.044.
[81] L. Shi, R. Liu, Y. Tang, J. Wang, Z. Wang, G. Cheng, M. Hu, Y. Yang, J. Ding, Hollow porous $Co_{0.85}Se$/ZnSe@MXene anode with multilevel built-in electric fields for high-performance sodium ion capacitors, Inorg. Chem. 63 (2024) 22923–22934, https://doi.org/10.1021/acs.inorgchem.4c04021.
[82] R. Sun, F. Xu, C. Wang, S. Lu, Y. Zhang, H. Fan, Rational design of metal selenides nanomaterials for alkali metal ion (Li^+, Na^+, K^+) batteries: current status and perspectives, Rare Met 43 (5) (2024) 1906–1931, https://doi.org/10.1007/s12598-023-02563-y.
[83] X. Qi, C.Y. Zhang, J. Yu, C. Huang, A. Yu, Q. Xue, C. Li, K. Li, X. Lu, Y. Ren, X. Bi, C. Zhang, J. Li, J.Y. Zhou, J. Arbiol, X. Qi, A. Cabot, Rapid electron transfer in $Co_{0.85}Se$-$MoSe_2$/NCP heterostructure catalyst towards robust lithium-sulfur batteries, J. Energy Chem. 106 (2025) 852–863, https://doi.org/10.1016/j.jechem.2025.03.028.
[84] C. Zhang, J. Yang, H. Li, M. Su, B. Xiong, F. Gao, Q. Lu, Multi-layered heterogeneous interfaces created in $Co_{0.85}Se$@Ni_3S_4/NF to enhance supercapacitor performances by multi-step alternating electrodeposition, Dalton Trans. 53 (2024) 13087–13098, https://doi.org/10.1039/d4dt01118j.
[85] S. Wu, F. Wu, Y. Li, C. Liu, Y. Zhang, H. Fan, Synergistically enhanced sodium ion storage from encapsulating highly dispersed cobalt nanodots into N, P, S tri-doped hexapod carbon framework, J. Colloid Interface Sci. 649 (2023) 741–749, https://doi.org/10.1016/j.jcis.2023.06.159.